J. Non-Newtonian Fluid Mech. 165 (2010) 652–671

Contents lists available at ScienceDirect

Journal of Non-Newtonian Fluid Mechanics

journal homepage: www.elsevier.com/locate/jnnfm

Efficient microfluidic rectifiers for viscoelastic fluid flow

P.C. Sousa [a], F.T. Pinho [b], M.S.N. Oliveira [a], M.A. Alves [a,*]

[a] Departamento de Engenharia Química, CEFT, Faculdade de Engenharia da Universidade do Porto, Rua Dr. Roberto Frias, 4200-465 Porto, Portugal
[b] Departamento de Engenharia Mecânica, CEFT, Faculdade de Engenharia da Universidade do Porto, Rua Dr. Roberto Frias, 4200-465 Porto, Portugal

ARTICLE INFO

Article history:
Received 6 December 2009
Received in revised form 18 March 2010
Accepted 18 March 2010

Keywords:
Microfluidic rectifier
Microfluidics
Viscoelastic fluid flow
Diodicity
Extensional flow
Elastic instabilities

ABSTRACT

In this work we propose a new type of microfluidic rectifier, which is able to operate efficiently under creeping flow conditions. The flow of Newtonian and non-Newtonian fluids was investigated experimentally in different microchannels with triangular (nozzle/diffuser) and hyperbolic shapes in order to achieve high anisotropic flow resistance between the two flow directions. The Newtonian fluid used was de-ionized water and the viscoelastic fluids were aqueous solutions of polyacrylamide and polyethylene oxide with different molecular weights. Pressure drop measurements were performed in addition to visualizations of the flow patterns by streak line photography for a wide range of flow rates. For the Newtonian flows, inertia leads to the appearance of recirculations for both flow directions, but no significant rectification effects appear. For the viscoelastic fluids, two distinct behaviors are identified: at low flow rates, the pressure drops are similar in both flow directions; above a critical flow rate (or Deborah number), the flow patterns become quite different, leading to different flow rates in the forward and backward flow directions for the same pressure drop, i.e., rectification effects emerge. In particular, the viscoelastic fluid flow becomes unsteady in the forward direction, due to the presence of elastic instabilities, which leads to a significant increase in the flow resistance. Flow resistance ratios greater than three were achieved for the hyperbolic rectifier, clearly in excess of the value for the triangular-shaped rectifier and for other geometries proposed in the literature for operation in creeping flow conditions. This high diodicity is associated with the distinct nature of the extensional flows in the forward and backward directions of the hyperbolic-type microgeometry.

1. Introduction

Today, the lab-on-a-chip concept has widespread application in science and technology, as in biology, medicine and engineering. Miniaturized systems for dispensing therapeutic agents, analysis of drugs or DNA molecules, microchemical reactors or inkjet printing heads are just a few examples of microfluidics applications. These devices handle small-sized samples, making portability a relevant characteristic of these miniaturized laboratories. In micro total analysis systems (μTAS), small and precise fluid volumes with well defined fluid properties and flow characteristics (i.e. viscosity, density, pH, temperature, etc.) must be pumped, transported, controlled or handled using external devices such as pumps, valves or other actuators.

Positive displacement pumps are the primary selection in microfluidics given their typical low Reynolds numbers flows. These devices require valves at the inlet and outlet and also between chambers in multi-chamber pumps, which poses a complex challenge in the miniaturization of pumping systems [1] and an increase in their effective cost and risk of failure [2]. These valves may also have detrimental effect upon cells, molecules and other entities sensitive to damage, which in some cases must be avoided. Therefore, and as an alternative to the use of active or passive valves, microchannels with a fixed geometry and direction-dependent flow resistance are used. These so-called flow rectifiers are the fluid mechanics equivalent of electronic diodes; pumps equipped with such devices are frequently encountered in microfluidics, where they are called valveless micropumps, also known as no-moving parts (NMP) or fixed geometry micropumps, and have received broad attention and various optimized geometries have been developed and tested when operating with Newtonian fluids [3]. Note also that in some micropumps the actuator is placed in the middle of the flow rectifier.

One of the earliest reciprocating displacement micropumps was developed by Jan Smits in the 1980s for controlled delivery of insulin to diabetics, as an alternative to classical delivery systems [4]. Since then, several micropump designs have been developed and investigated (e.g. [2,5–8]) and the vast majority do contain some inlet/outlet valves or NMP flow rectifiers.

The first flow rectifier, named "Valvular conduit", was proposed and patented by Tesla [9] and consisted of an open main duct

* Corresponding author. Tel.: +351 225081680; fax: +351 225081449.
E-mail addresses: psousa@fe.up.pt (P.C. Sousa), fpinho@fe.up.pt (F.T. Pinho), monica.oliveira@fe.up.pt (M.S.N. Oliveira), mmalves@fe.up.pt (M.A. Alves).

0377-0257/$ – see front matter © 2010 Elsevier B.V. All rights reserved.
doi:10.1016/j.jnnfm.2010.03.005

Table 1
Summary of previous studies regarding no-moving parts micropumps.

Ref.	Valve material/type	Application	Exp/Num	Fluid	ΔP_{max} (kPa)	Diodicity/efficiency	Re_{max}	Notes
[1]	Silicon-glass, diffuser/nozzle, Tesla-type	Valv. micr. (PZT actuator)	Exp/Num	Newtonian (water)	30.4	1.2	n.r.	2D and 3D simulations; best diodicity for diffuser valve
[7]	Silicon-glass, diffuser/nozzle	Valv. micr. (thermopneumatic actuator)	Exp	Newtonian (water)	2.5	n.a.	n.r.	The maximum flow rate of the micropump is 0.014 ml/min
[8]	n.a., diffuser/nozzle	Valv. micr. (PZT actuator)	Num	Newtonian (water)	n.r.	n.r.	n.r.	Theoretical analysis and numerical simulations; maximum pump flow rate of 0.08 ml/min
[10]	Brass, diffuser/nozzle	Valv. micr.	Exp	Newtonian (water)	19.6	2	10^3	Maximum pump flow rate of 16 ml/min
[11]	Brass, diffuser/nozzle	Valv. micr. (PZT actuator)	Exp	Newtonian (water)	16	2	n.r.	Double chamber pump; comparison between experimental and theoretical results; maximum net flow rate of 16 ml/min
[12]	Silicon-glass, diffuser/nozzle	Valv. micr.	Exp	Newtonian (methanol/water)	100	1.45	~200	Different open angles and different dimensions were studied; maximum efficiency for methanol; experimental and analytical results are compared
[13]	Silicon, diffuser/nozzle	Valv. micr.	Exp/num	Newtonian (water)	1	1.5	10^5	Different open angles and conical structures were studied; maximum net flow rate of 0.028 ml/min
[14]	n.a., diffuser/nozzle	Valv. micr.	Analytical	Newtonian	n.a.	n.a.	n.a.	Derivation of a model for the fluid flow; dimensionless analysis
[15]	Silicon, diffuser/nozzle	Valve	Exp	Newtonian (water)	n.r.	1.725	400	Different opening angles and depths were studied; max. diodicity for an open angle of 30°; fixed flow rate in all experiments
[16]	n.a., diffuser/nozzle	Valv. micr.	Num	Newtonian (water/methanol)	n.r.	1.43	10^3	Planar, pyramidal and conical geometries studied
[18]	Silicon, diffuser/nozzle	Valve	Exp	Newtonian (water)	0.6	1.5	22	Best efficiency obtained at an open angle of 30°
[19]	Stainless steel, diffuser/nozzle	Valv. micr. (PZT actuator)	Exp	Newtonian (water/water + glycerol)	1.4	n.r.	10^3	Different opening angles were studied
[20]	Epoxy-glass, diffuser/nozzle	Valv. micr. (PZT actuator)	Exp/num	Newtonian (water)	n.r.	n.r.	n.r.	Comparison between experimental and theoretical results
[21]	Aluminium, diffuser/nozzle	Valv. micr.	Exp/num	Newtonian (water)	n.r.	2	2×10^3	Studied different opening angles (best efficiency at 40°)
[22]	n.a., diffuser/nozzle	Valv. micr. acoustic	Num	Newtonian (water)	10	~1.3	51	Pulsating flow; studied different angles; maximum rectification effect at 60°
[23]	Silicon-glass, diffuser/nozzle	Valv. micr. (PZT actuator)	Exp	Newtonian (water/methanol)	7	n.r.	10^4	Maximum pressure drop for methanol
[24]	Silicon, diffuser/nozzle	Valve	Exp	Newtonian (water)	80	Diffuser/nozzle 29%	n.r.	3D structures; different open angles and different dimensions were studied
[25]	Micromachined, diffuser/nozzle	Valv. micr.	Exp/num	Newtonian (water)	~200	1.59 (Exp), 3.20 (2D Num)	1350 (Num), 650 (Exp)	Structures with round inlets and sharp outlets; 2D and 3D simulations; experimental study of various geometrical dimensions
[27]	Silicon, diffuser/nozzle	Valv. micr. (PZT actuator)	Exp	Newtonian (water)	1.2	n.r.	n.r.	Diffuser/nozzle structures used as obstacles in a micropump
[29]	n.a., Tesla	Valv. micr.	Analytical	Newtonian	n.a.	n.a.	n.a.	Geometry-based model for analysis of no-moving parts microvalves; Experimental data reported in the literature is used
[30]	Acrylic, Tesla	Valv. micr.	Exp/num	Newtonian	20	1.5	2×10^3	Shape was optimized using CFD tools; experiments carried out using the optimized geometry.
[31]	PMMA, diffuser/nozzle	Valv. micr. (electromagnetic actuator)	Exp/num	Newtonian (water/air)	2	2	27	Studied sharp and round corners; pump flow rate of 0.4 ml/min and 12 mbar
[34]	PDMS, flap	Valv. micr.	Exp	Newtonian (water)	8	3.9	n.r.	Flap valve that works as a rectifier
[35]	PDMS, flap	Valve	Exp.	Newtonian (water)	14	4.6	30	Different valve heights were studied

Table 1 (*Continued*)

Ref.	Valve material/type	Application	Exp/Num	Fluid	ΔP_{max} (kPa)	Diodicity/efficiency	Re_{max}	Notes
[36]	Silicon-glass, diffuser/nozzle	Valv. micr. (PZT actuator)	Exp	Newtonian fluids used in biochemistry	n.r.	n.r.	n.r.	Tested different fluids that cannot be pumped in other micropumps, such as high ionic character fluids and cell suspensions; maximum flow rate of 0.014 ml/min
[37]	PDMS, diffuser/nozzle	Valve	Exp	Viscoelastic (PAA)	11	2	1.4	Rectifier with 43 similar elements in series
[40]	Silicon-glass, diffuser/nozzle	Valve	Exp	Viscoelastic (PEO)	100	1.8	20	Rectifier with 10 similar elements; different dimensions and angles of the walls were studied

Valv. micr., valveless micropump; PZT, piezoelectric; CFD, computational fluid dynamics; Exp., experimental; Num., numerical; n.a., not applicable; n.r., not reported; PAA, polyacrylamide; PDMS, polydimethylsiloxane; PEO, polyethylene oxide; PMMA, polymethylmethacrylate.

connected to a series of side loop channels at sharp angles. Its rectification effects were found for Newtonian fluids at moderate Reynolds numbers (Re), when nonlinearities due to inertial effects became important. Stemme and Stemme [10] proposed a nozzle/diffuser micropump with a fixed geometry, which consists of a channel with opening angles that work as flow-directing elements. When Newtonian fluids flow in the diverging wall direction (diffuser element), enhanced flow-directing properties are achieved and the pressure drop becomes dependent on the flow rate. This nozzle/diffuser geometry became a very popular flow rectifier design. In order to optimize the corresponding valveless micropumps, Olsson et al. [11] investigated, from a theoretical and experimental point of view, the planar nozzle/diffuser structure of a double chamber brass based micropump. Other contributions to the optimization of the nozzle/diffuser performance have been carried out numerically and experimentally over the last decade (e.g. [8,12–22]). Gerlach and Wurmus [23] studied a piezoelectrically driven micropump in which a nozzle/diffuser valve was incorporated and concluded that the device could be used as a mixer/reactor chamber, in addition to operating as a micropump, due to the turbulence that was generated during its operation. Forster et al. [1] tested and compared the efficiency of different NMP valves, a simple diffuser and a valvular conduit (Tesla-type). In the end, the Tesla-type valve was found to have the highest difference between forward and backward flow resistance, an important flow property called diodicity.

Three-dimensional (3D) nozzle/diffuser microvalves etched in silicon were investigated by Heschel et al. [24]. Devices with different dimensions and shapes were tested and it was found that the flow behavior within 3D nozzle/diffuser microstructures depends only weakly on the shape of the geometry, with higher improvements in efficiency brought by rounding the throat. Olsson et al. [25] reported a numerical and experimental investigation of nozzle/diffuser elements for valveless micropumps. The sharpness of the throat corner edges was explored in their study and the flow-directing capability of the geometry was demonstrated. At low Reynolds numbers, the 3D simulations predicted well the difference between the pressure drops for each flow direction, whereas at high Reynolds numbers good results could only be achieved using a two-dimensional numerical code. Nozzle/diffuser geometries were also used in valveless micropumps embedded as asymmetric obstacles within a piezoelectrical micropump [26,27]. The Tesla-type valves were used in several studies as a NMP microdevice or coupled in micropumps, similar to the device used by Forster et al. [1]. More recently, the geometry of these valves has been optimized for high Reynolds number Newtonian flow [28–30].

Micropumps, valves and flow rectifiers can be fabricated in diverse materials using straightforward and inexpensive methods [31]. Photocurable polymers, such as hydrogels that can be photopolymerized in situ, were explored [32,33]. Loverich et al. [34] reported a polymer-based micropump fabricated with transparent (for optical access), fluid-compatible and economical materials. This micropump integrated an elastomeric actuator and flap check valves, made up of PDMS (polydimethylsiloxane), that conditioned the flow behavior generating a dependency between the pressure drop across the microvalve and the flow rate. More recently, Loverich et al. [35] reported an improved flap check valve for operation at low Reynolds number flow having a maximum pressure drop ratio of 4.6 between the two flow directions and for the same flow rate. In medical or biological μTAS chips, it is very important to preserve the characteristics of the fluid that is being pumped (e.g. biological fluids) and passive or active check valves frequently are not the best choices. Instead, NMP valves have the lowest detrimental effect upon the biological entities in the fluid. A valveless micropump for pumping fluids, containing beads and living cells, without damage was developed by Andersson et al. [36].

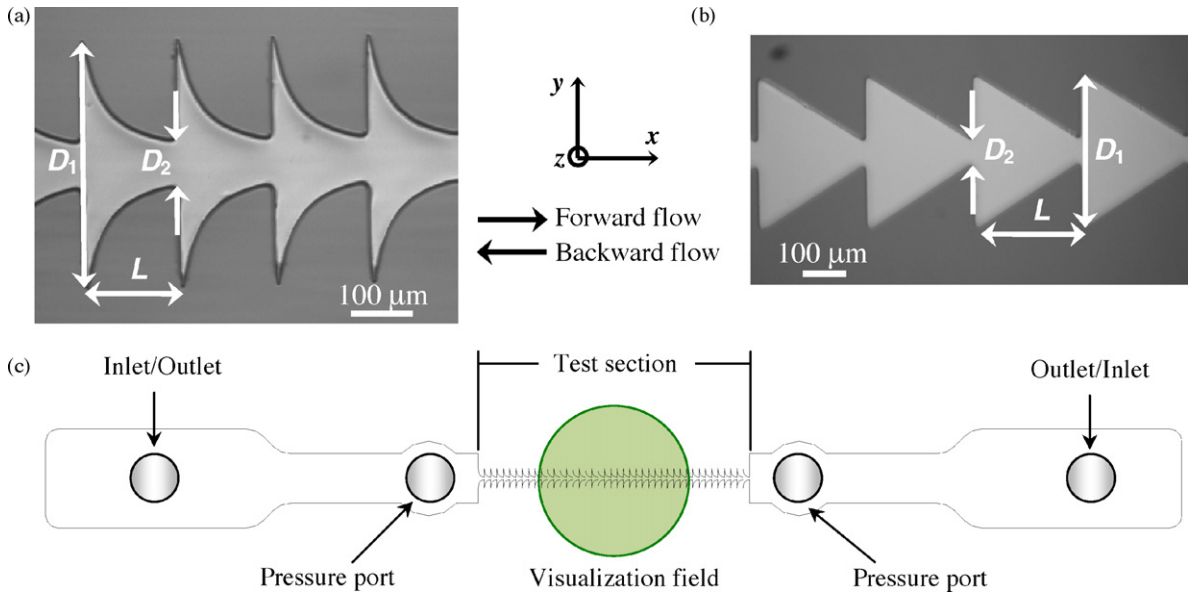

Fig. 1. Micrograph of the (a) hyperbolic and (b) triangular-shaped microfluidic rectifiers. (c) Top view of the microchannel used in the experiments.

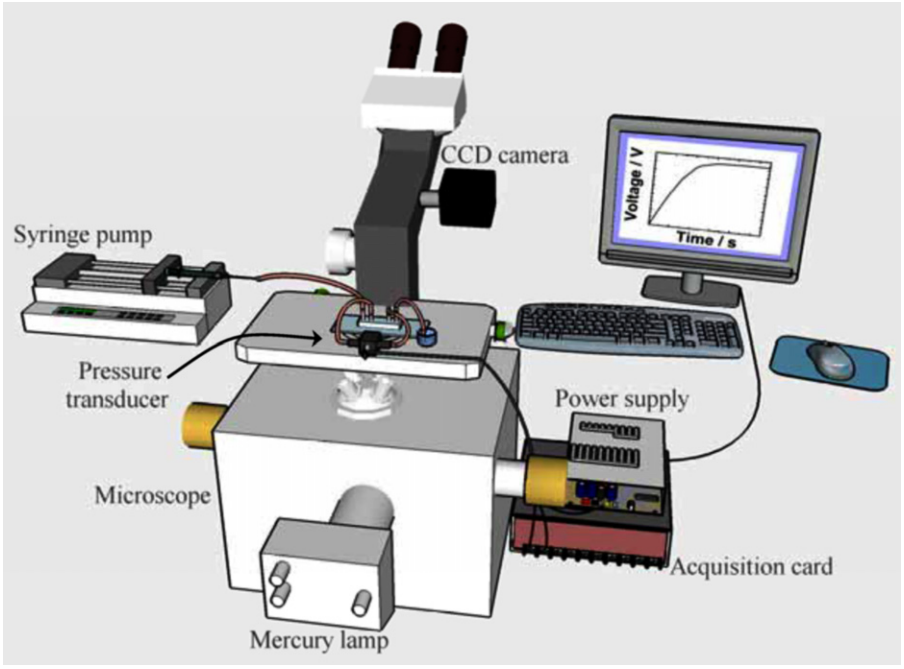

Fig. 2. Schematic view of the experimental set-up.

All investigations discussed so far refer to Newtonian fluid flow, usually using water. For Newtonian fluids the rectification effect of NMP devices is a consequence of the flow inertia. However, microfluidic flows typically occur under low Reynolds number flow conditions and as such, the flow resistance is only weakly dependent, or even independent, of the flow direction due to the reversibility of creeping flows of Newtonian fluids (i.e. rectification effects are small). Nevertheless, anisotropic flow resistance can be

Table 2
Geometrical characteristics of the microchannels studied.

Channel	D_1 (μm)	D_2 (μm)	L (μm)	Hencky strain, ε_H	a (μm^2)	b (μm)
Triangular, T	330	37	230	2.19	–	–
Hyperbolic						
C_1	400	54	128	2.00	4000	20
C_2	326	37	230	2.18	4800	29
C_3	390	54	382	1.98	11972	61
C_4	400	20	382	3.00	4000	20

Table 3
Properties of the fluids used.

Fluid	M_w (g mol^{-1})	Polymer (ppm)	Water (%)	Sucrose (%)	NaCl (%)	Glycerol (%)	ρ (kg m^{-3})
Newtonian	–	–	100	–	–	–	998
PEO-2M	2×10^6	1000	99.90	–	–	–	998
PEO-8M	8×10^6	1000	99.90	–	–	–	998
PEO-8M + Glyc.	8×10^6	1000	59.90	–	–	40.00	1099
PEO-8M 100	8×10^6	100	99.99	–	–	–	999
PAA	18×10^6	100	85.91	13.06	1.02	–	1059

Table 4
Initial and final aspect ratios used in CaBER experiments and measured relaxation times (T = 293.2 K).

Fluid	Λ_i	Λ_f	λ (ms)
PEO-2M	0.33	1.34	8.2 ± 0.8
PEO-8M	0.50	1.39	73.9 ± 1.0
PEO-8M + Glyc.	0.50	1.63	17.9 ± 0.6
PEO-8M 100	0.33	1.19	2.5 ± 0.2
PAA	0.50	1.50	13.2 ± 0.2

Table 5
Coil overlap concentration, dimensionless concentration and Zimm relaxation times for each fluid used in the experiments.

Fluid	c^* (g cm^{-3})	c/c^*	λ_{Zimm} (ms)
PEO-2M	8.58×10^{-4}	1.16	0.63
PEO-8M	3.48×10^{-4}	2.86	10.1
PEO-8M + Glyc.	3.48×10^{-4}	3.15	21.8
PEO-8M 100	3.48×10^{-4}	0.29	3.36
PAA	5.12×10^{-4}	0.21	10.3 ± 0.5

Table 6
Rheological parameters of the PTT model at the reference temperature (T_0 = 293.2 K), and parameter $\Delta H/R$ for the fluids used. The relaxation times are presented in Table 4.

Fluid	η_0 (mPa s)	η_s (mPa s)	ε	$(\Delta H/R)$ (K)
PEO-2M	2.55	1.9	0.05	2.84×10^3
PEO-8M	7.50	3.0	0.04	2.98×10^3
PEO-8M + Glyc.	10.5	6.5	0.04	2.18×10^3
PEO-8M 100	1.15	1.0	0	2.31×10^3
PAA	2.34	2.0	0.1	1.76×10^3

achieved under creeping flow conditions providing other nonlinear mechanisms come to play a role. One possible alternative relies on adding small amounts of additives that confer viscoelastic rheological properties to the fluid [37]. Since viscoelastic nonlinearities can be enhanced at the microscale [38], rectification effects can be achieved even with dilute polymeric fluids. The elasticity number, which represents the relative importance of elastic to inertial effects and is given by the product of relaxation time and kinematic viscosity divided by the length scale squared, increases as the size of the geometry is reduced, thus demonstrating the importance of elastic effects in microfluidics as compared to the macroscale. A pioneering investigation on viscoelastic flows at the microscale was undertaken by Groisman et al. [39]. The flow of dilute aqueous polyacrylamide (PAA) solutions in a complex nonlinear resistor was studied, demonstrating the potential for use as a flow stabilizer (the flow rate across the microfluidic device is approximately constant for a large range of applied pressure drops), due to the elastic nature of the working fluid.

Somewhat surprisingly, studies that describe microfluidic rectifiers with non-Newtonian fluid flows are scarce. Groisman and Quake [37] investigated the flow of a 0.01 wt.% aqueous solution of a high molecular weight PAA, through a microchannel with a nozzle/diffuser structure composed of a consecutive number of similar triangles (cf. Fig. 1b). Anisotropic flow resistance was observed and a maximum flow rate ratio of almost 2 was achieved for the same pressure gradient applied in both flow directions. Nguyen et al. [40] also investigated the rectification effects at low Re in a similar nozzle/diffuser structure using an aqueous solution of polyethylene oxide (PEO) at 0.1 wt.%. They studied the effect of the opening angle of the triangular structures on the flow resistance anisotropy and found a maximum rectification effect characterized by a flow rate ratio of about 1.8.

A list summarizing relevant investigations on flows of Newtonian and non-Newtonian fluids in systems including valveless micropumps or flow rectifiers is presented in Table 1, where the above referenced works are also listed. This table includes information on the type of investigation, materials used, flow geometry,

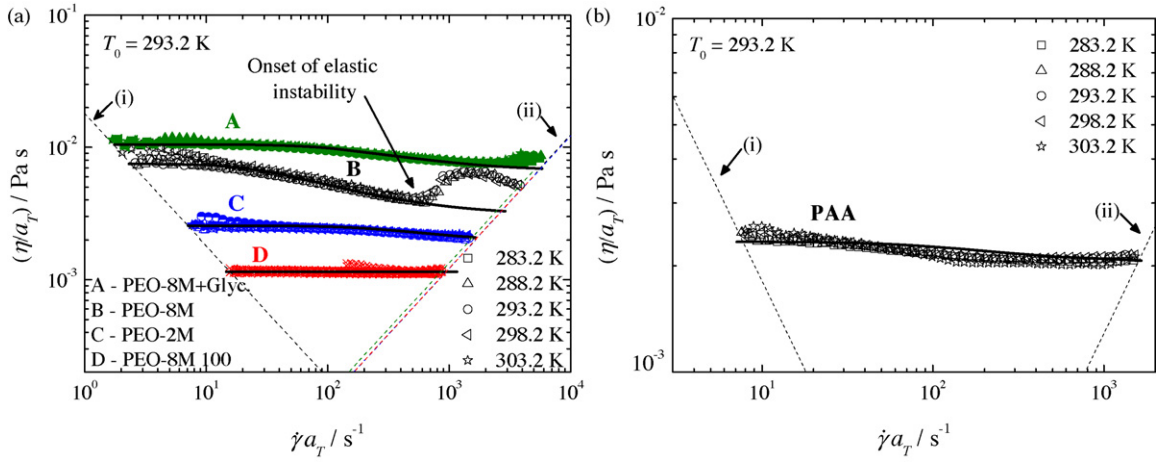

Fig. 3. Master curves of the steady shear viscosity: (a) PEO solutions; (b) PAA solution. The solid lines represent the PTT model fittings for each fluid. (i) Minimum measurable shear viscosity calculated from 20× the minimum measurable torque of the rheometer; (ii) onset of secondary flow due to Taylor instabilities (two distinct lines are drawn in (a) corresponding to different fluid densities).

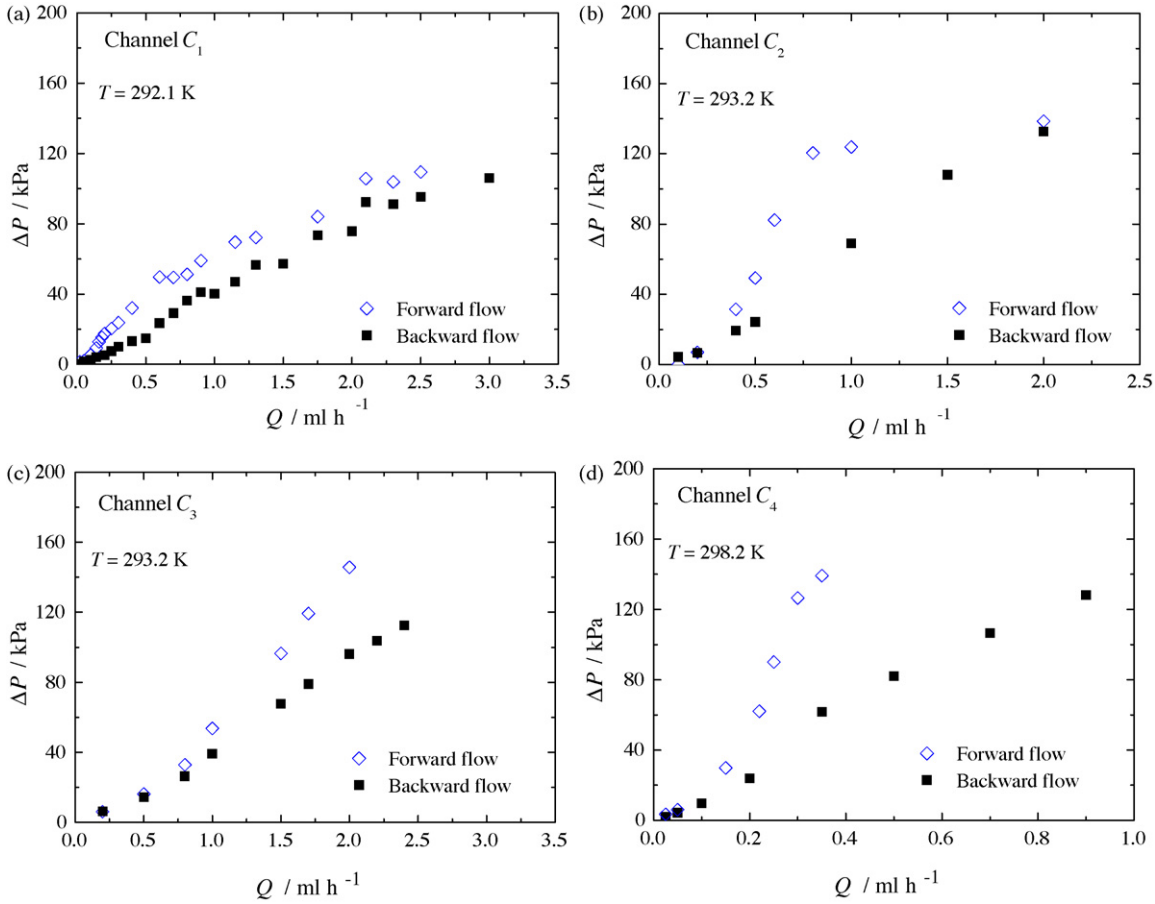

Fig. 4. Pressure drop measured with the PEO-8M fluid in the forward and backward flow directions for a range of flow rates in different hyperbolic microchannels: (a) C_1 at 292.1 K; (b) C_2 at 293.2 K; (c) C_3 at 293.2 K; (d) C_4 at 298.2 K.

maximum pressure drop across the device, Reynolds number range and the achieved diodicity, in addition to some relevant comments.

It is clear that there is much to be explored in this area of flow rectifiers for creeping flows operating with polymer additives and this paper is one such contribution. Here, we investigate the performance of microfluidic no-moving parts rectifiers having a hyperbolic-like shape, which are able to operate efficiently under creeping flow conditions using dilute viscoelastic polymeric solutions. The main objective is to design an efficient microgeometry with high rectification effects. Using Newtonian and non-Newtonian fluids, the performance of the optimized geometry was compared with that of the nozzle/diffuser structure of Groisman and Quake [37] and Nguyen et al. [40] by means of flow rate and pressure drop measurements, in addition to visualizations of the flow patterns. The microfluidic rectifiers were fabricated in PDMS using a low cost soft lithography technique and are composed of a succession of contractions/expansions with different hyperbolic and triangular shapes.

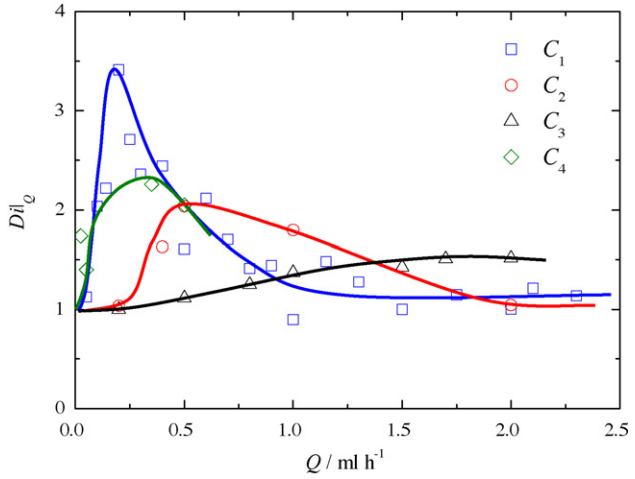

Fig. 5. Diodicity obtained for the flow rate range studied in the four microchannels with hyperbolic shaped elements using PEO-8M fluid. The lines are a guide to the eye.

The remainder of this paper is organized as follows: Section 2 describes the flow geometries, their fabrication and the experimental techniques used. In Section 3 the working fluids and their rheology are presented, followed by a discussion of the dimensionless groups that characterize the flow to set the stage for the experiments, the results of which are presented and discussed in Section 4. The paper closes with conclusions in Section 5.

2. Experimental techniques

2.1. Microchannels geometry, fabrication and experimental set-up

The microchannels used in the experiments were fabricated in PDMS using standard soft lithography techniques [41] and SU-8 photo-resist molds. PDMS elastomer has been widely used for the fabrication of microfluidic devices because of its characteristics such as transparency, mechanical behavior, biocompatibility, rapid prototyping and low cost. In this work, two different types

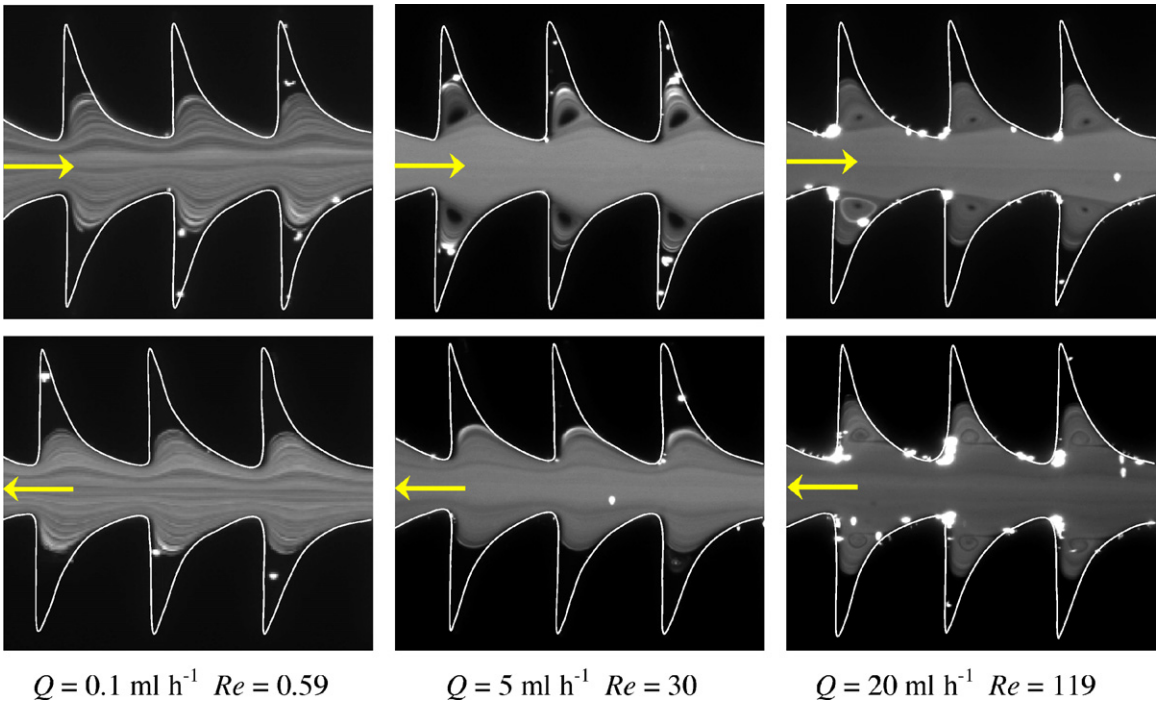

Fig. 6. Flow patterns for Newtonian fluid (de-ionized water at $T = 296.2$ K) flow. Top images correspond to forward flow and bottom images correspond to backward flow in microchannel C_1.

of planar microgeometries were used: one composed of triangular elements, based on the nozzle/diffuser structure reported in the literature [25,37,40] and another type of microchannels with hyperbolic shaped elements. Fig. 1 illustrates the layout of two typical microchannels used in this work.

All microgeometries used consist of a sequence of 42 similar elements aligned in series. The hyperbolic shape was selected in order to achieve fluid flows that are primarily extensional, with a nearly constant strain rate along the centerline, as discussed by Oliveira et al. [42]. We define the forward direction when the fluid flows along smooth contractions and abrupt expansions (left to right in Fig. 1) and backward direction as the opposite one. For the forward flow the fluid is stretched at a nearly constant extensional rate along the centerline, resulting in a high flow resistance for fluids that have large extensional viscosities, such as solutions of high molecular weight polymers, whereas in the backward flow direction the fluid can relax also at a nearly constant extensional rate.

The devices used in the present investigation are composed of two inlets/outlets located at the extremes of the microchannels, followed by pressure taps on each side of the test section, which is positioned at the central part of the microchannel, as shown in Fig. 1c. The pressure taps allow for the measurement of the pressure drop (ΔP) across the 42 repeating elements of the test section. Table 2 summarizes the dimensions of the different microgeometries used in the experiments, as well as the values of the Hencky strain (total deformation) experienced by the fluid, here defined as $\varepsilon_H = \ln(D_1/D_2)$. The parameters of the hyperbolic function that describes the shape of the microchannel elements, $y = \pm a/(x+b)$, where $0 \le x \le L$, are also listed in Table 2. At the widest and narrowest parts, the widths of the microgeometries are D_1 and D_2, respectively, and the length of each element is L, as sketched in Fig. 1. The depth of the channels is uniform and was kept constant for all micro-devices studied, $h = 50\ \mu$m.

In order to make a direct comparison between the results obtained with the hyperbolic rectifier proposed in this work and the triangular rectifier geometry investigated by Groisman and Quake [37] it is necessary to use microgeometries with similar aspect ratios. For that purpose the triangular rectifier and the C_2 hyperbolic rectifier used in this work have similar dimensions.

The flow behavior of Newtonian and non-Newtonian fluids was studied at room temperature in the forward and backward directions (cf. Fig. 1) for a wide range of flow rates, which were imposed using a syringe pump (PHD2000, Harvard Apparatus). Syringes (Hamilton) with volumes ranging from 50 μl to 10 ml were used according to the desired flow rate and connected to the microchannels via Tygon tubing of 0.44 mm internal diameter. The outlet of the microchannels was connected to Tygon tubing that directs the fluid to a reservoir open to the atmosphere where the fluid is collected.

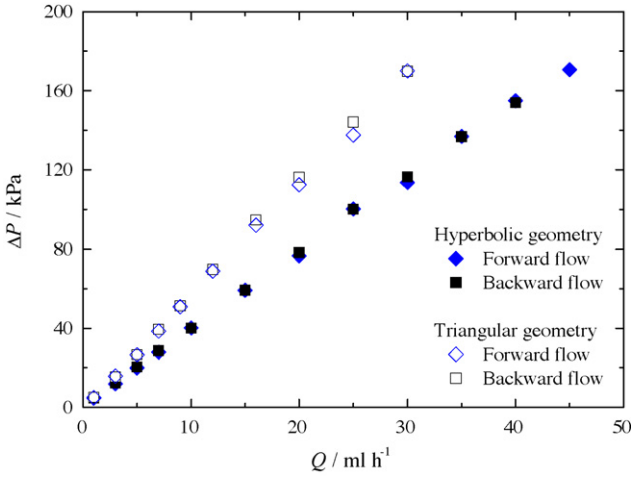

Fig. 7. Pressure drop measured as a function of flow rate for the Newtonian fluid (de-ionized water) flow in the microchannel with a hyperbolic shape, C_1 (solid symbols) at 295.7 K and in the microchannel with a triangular shape, T (open symbols) at 298.5 K.

2.2. Flow visualization

Visualizations of the flow patterns relied on streak line photography. For this purpose, the fluids were seeded with 1 μm fluorescent tracer particles (Nile Red, Molecular Probes, Invitrogen, Ex/Em: 520/580 nm) and sodium dodecyl sulfate (0.1 wt.%, Sigma–Aldrich) was added to the solutions in order to reduce the adhesion of fluorescent particles to the channel walls. Rheological measurements confirmed that the rheology of the fluid was not changed by using such low concentrations of this surfactant agent. The optical setup is shown schematically in Fig. 2. It consists of an inverted epi-fluorescence microscope (Leica Microsystems GmbH, DMI 5000M) equipped with a CCD camera (Leica Microsystems GmbH, DFC350 FX), a filter cube (Leica Microsystems GmbH, excitation BP 530–545 nm, dichroic 565 nm, barrier filter 610–675 nm) and a 100 W mercury lamp light source.

The microgeometries were continuously illuminated and path line images were acquired using a 10× (NA = 0.25) microscope objective (Leica Microsystems GmbH) and long exposures times (~1 s) in order to obtain a visual fingerprint of the flow patterns in the focused center plane. The depth of field (DOF) for an optical system can be calculated as [43]:

$$\delta z = \frac{n\lambda_0}{(NA)^2} + \frac{ne}{(NA)M} \quad (1)$$

where n is the refractive index, λ_0 is the wavelength of the light (in vacuum), NA is the numerical aperture of the objective, e is the minimum detectable size and M is the total magnification. For our optical set-up, $\delta z = 12$ μm and $e/M = 0.65$ μm, which is a value smaller than the particle diameter, d_p.

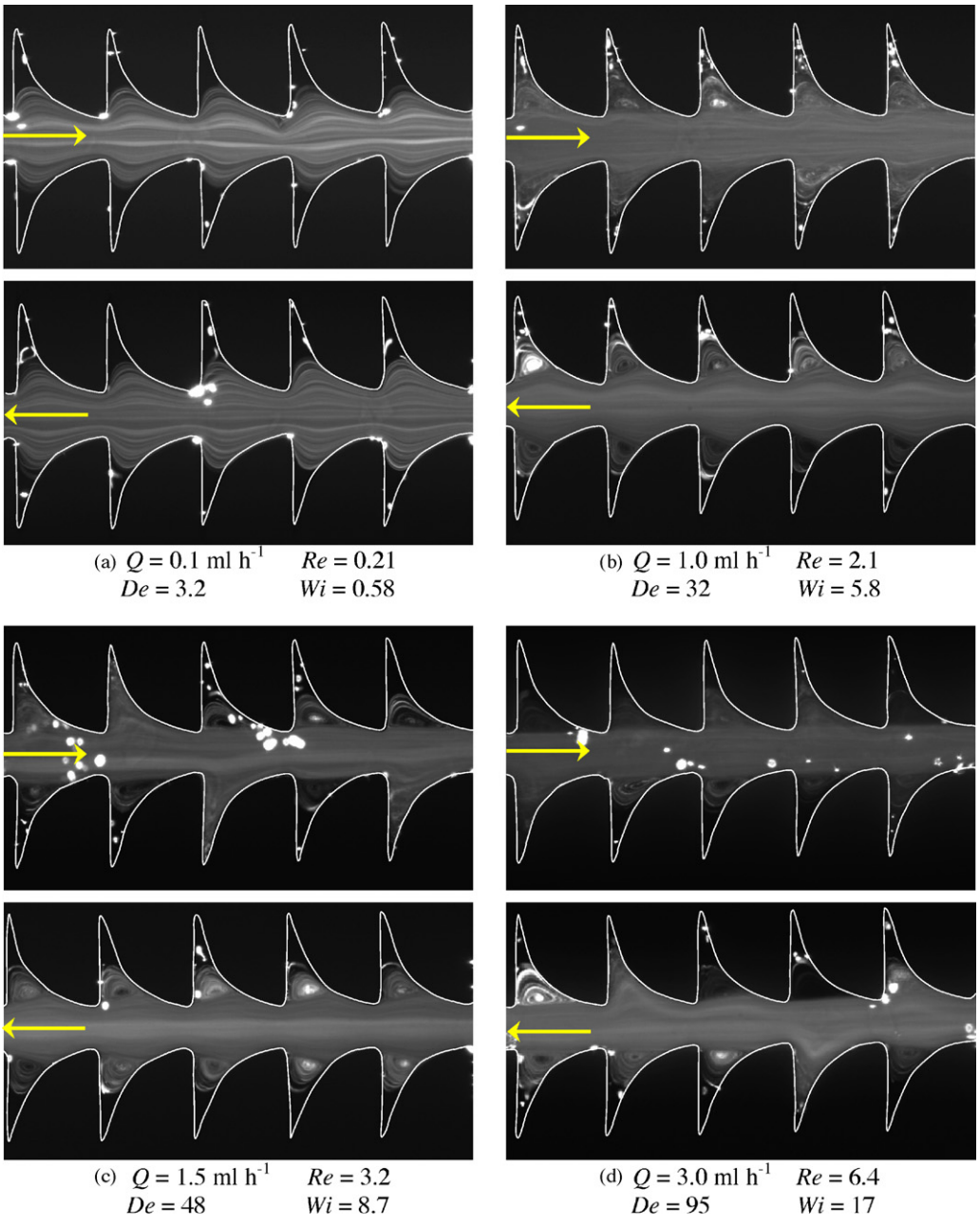

Fig. 8. Effect of elasticity on the flow patterns of the PEO-2M fluid (microchannel C_1) at 292.7 K.

2.3. Pressure drop measurements

Pressure drop measurements were performed using Honeywell differential pressure sensors (model 26PC series) covering values up to $\Delta P = 200$ kPa. The pressure sensors were calibrated using a static column of water for pressures up to $\Delta P = 34$ kPa and using a compressed air line and a manometer (Wika Instrument Corporation, model 332.50) with an accuracy of ± 2 kPa for sensors that are able to measure higher differential pressures, up to 200 kPa.

The ports of the pressure transducer were connected to two pressure taps, located upstream and downstream of the test section (cf. Fig. 1c), respectively. A 12 V DC power supply (Lascar electronics, PSU 206) was used to power the pressure sensors that were also connected to a computer via a data acquisition card (NI USB-6218, National Instruments) in order to record the output data using LabView v7.1. The transient response of the pressure sensors was continuously recorded until steady-state was reached.

3. Fluids and nondimensional numbers

3.1. Fluid composition and rheology

A Newtonian fluid (de-ionized water) and various viscoelastic fluids with different rheological behavior were used in the experiments. The polymers used to prepare the viscoelastic fluids were polyacrylamide with a molecular weight $M_w = 18 \times 10^6$ g mol^{-1} (Polysciences) and polyethylene oxide (PEO) with two different molecular weights: $M_w = 2 \times 10^6$ g mol^{-1} (PEO-2M) and $M_w = 8 \times 10^6$ g mol^{-1} (PEO-8M), both supplied by Sigma–Aldrich. Solutions were prepared by mixing the polymer into the solvent (de-ionized water, de-ionized water/glycerol or de-ionized water/sucrose solutions) at different concentrations, utilizing magnetic stirrers at low speeds, in order to avoid mechanical degradation of the polymer molecules. To prevent chemical degradation, all solutions were kept in a refrigerator and additionally PEO solu-

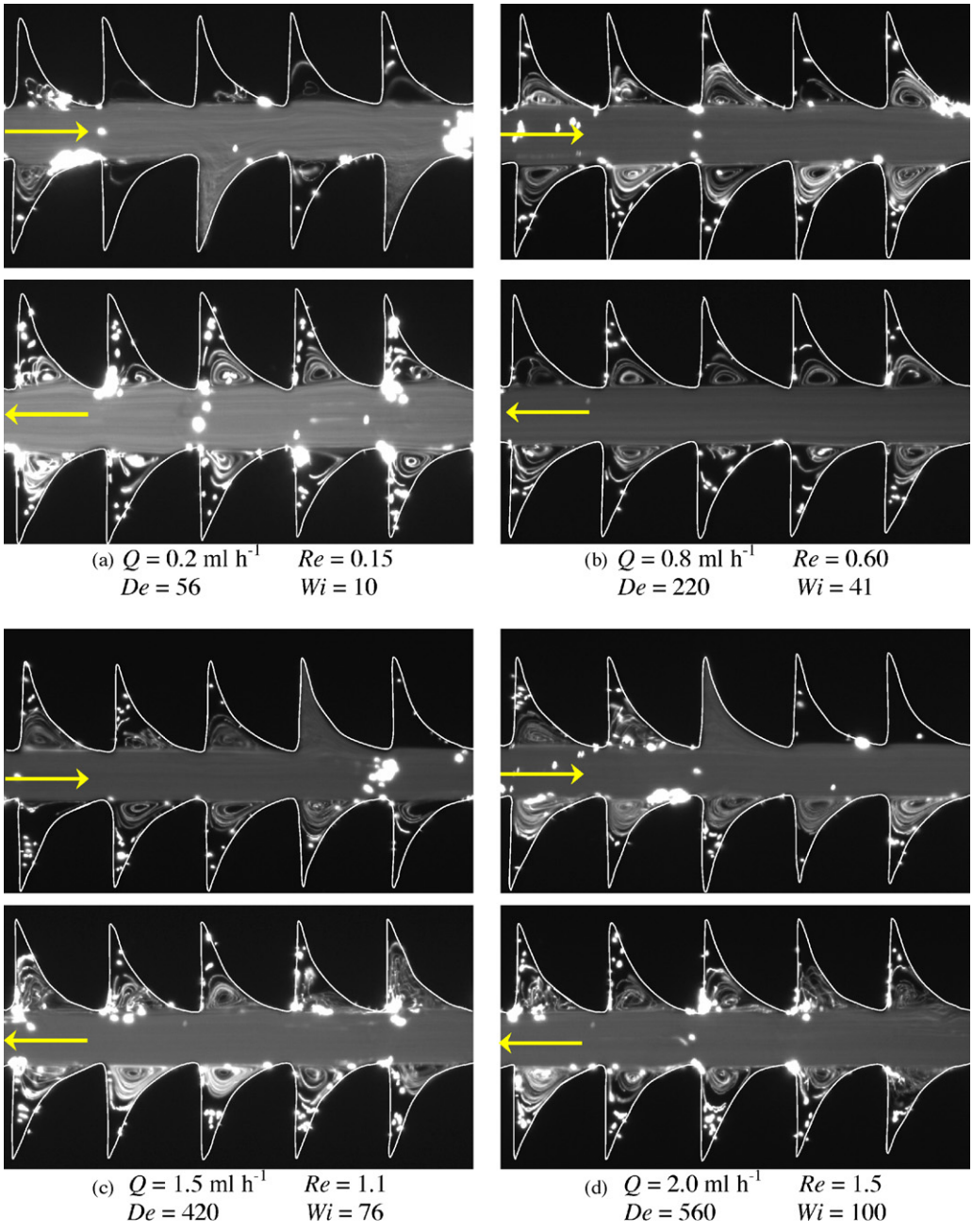

Fig. 9. Effect of elasticity on the flow patterns of the PEO-8M fluid (microchannel C_1) at 293.5 K.

tions were also protected from light using dark bottles [44]. The density of all solutions prepared was measured at 293.2 K using calibrated 5 cm^3 density flasks.

The composition of all fluids by weight, fluid density (ρ) and polymer molecular weight are given in Table 3.

The rheology of the fluids was measured in both extensional and shear flows. The extensional flow characterization used a capillary break-up extensional rheometer (Haake CaBER 1, Thermo Scientific) and the characteristic relaxation time of each fluid was measured. These measurements were performed using circular plates with a diameter $D_p = 6$ mm. The initial separation gap between the two plates was set to h_i, which corresponds to an aspect ratio, $\Lambda_i = h_i/D_p$. The liquid bridge confined between the two plates is stretched as the top plate moves linearly ($-50\,\text{ms} \le t \le 0$) to a final height ($h_f$), which leads to a final aspect ratio, $\Lambda_f = h_f/D_p$. In the ensuing liquid filament thinning the relaxation time, λ, was determined by fitting the experimental data of $\log[D(t)]$ vs time in the linear region to the equation resulting from the elasto-capillary balance [45]: $D(t)/D_0 \propto \exp[-t/(3\lambda)]$, where D_0 is the radius of the filament at time $t = 0$. In Table 4, we present the relaxation times obtained as well as the initial and final aspect ratios used for each viscoelastic fluid tested.

The critical overlap concentration, c^*, or the concentration at which adjacent polymer coils overlap, is calculated according to Graessley [46] as $c^* = 0.77/[\eta]$, where $[\eta]$ is the intrinsic viscosity.

The intrinsic viscosity for the PEO solutions can be estimated using the Mark–Houwink–Sakurada (MHS) equation, $[\eta] = 0.072\,M_w^{0.65}$ with $[\eta]$ expressed in cm^3/g [47]. The PEO-2M solution has an intrinsic viscosity, $[\eta] = 897\,cm^3/g$, while for the other PEO solutions with a molecular weight of $8 \times 10^6\,g\,mol^{-1}$

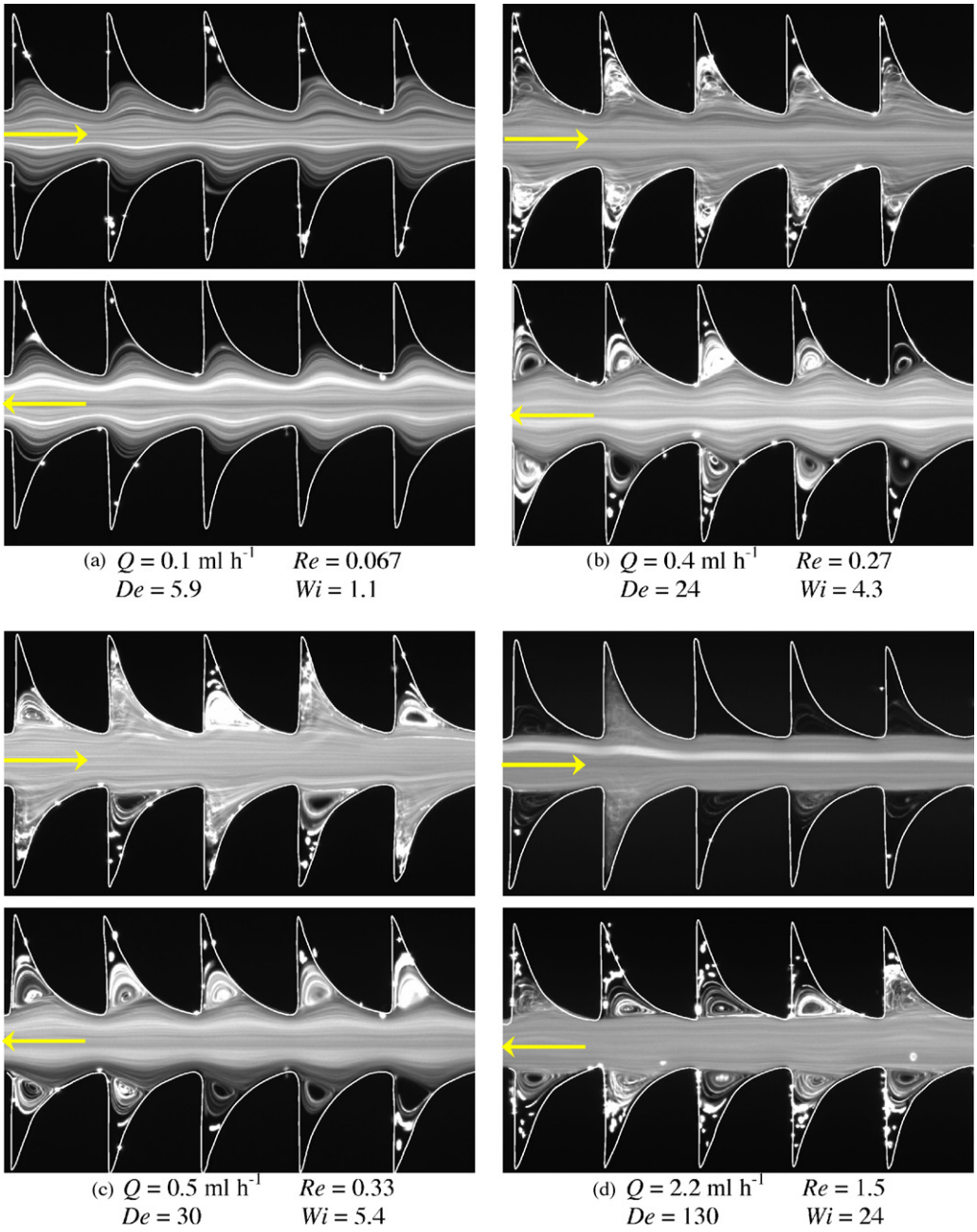

Fig. 10. Effect of elasticity on the flow patterns of PEO-8M + Glyc fluid (microchannel C_1) at 298.8 K.

the intrinsic viscosity is $[\eta] = 2210\,\mathrm{cm^3\,g^{-1}}$. The intrinsic viscosity of the PAA solution was determined experimentally using a Cannon-Fenske viscosimeter (Comecta SA, model 1464, size 50) and various dilute solutions with the same solvent and different polymer concentrations. The intrinsic viscosity was determined by means of an extrapolating method, namely using the Huggins equation, $(\eta - \eta_s)/(\eta_s c) = [\eta] + K_H[\eta]^2 c$, where η is the solution viscosity, η_s is the solvent viscosity, c is the concentration and K_H is the Huggins constant that measures the interaction between polymer and solvent [48]. The fit to the experimental data yields $[\eta] = 1504\,\mathrm{cm^3/g}$ and $K_H = 8.7$.

For a polymer chain in a good solvent, the longest relaxation time can be calculated according to the Zimm theory [49] as

$$\lambda_{\mathrm{Zimm}} = \frac{1}{\zeta(3\nu)} \frac{[\eta] M_w \eta_s}{N_A k_B T} \tag{2}$$

where N_A is Avogadro's number, k_B the Boltzmann constant, T the absolute temperature and $\zeta(3\nu) = \sum_{i=1}^{\infty}(1/i^{3\nu})$ represents the sum of individual modal contributions to the relaxation time. For the PEO solutions in water or in water/glycerol, the solvent quality exponent, ν, and the prefactor, $1/\zeta(3\nu)$ are 0.55 and 0.46 respectively, as reported elsewhere [45]. On the other hand, to the best of our knowledge, the solvent quality exponent reported in the literature for PAA solutions considers only water as the solvent, rather than water/sucrose. However, using these values we can obtain a crude estimate of the longest relaxation time (λ_{Zimm}) for comparative purposes. As such, considering water as the main solvent component, the exponent varies between $\nu = 0.61$ (for $4 \times 10^4 \le M_w/\mathrm{g\,mol^{-1}} \le 1.47 \times 10^6$) and $\nu = 0.57$ (for $4.9 \times 10^5 \le M_w/\mathrm{g\,mol^{-1}} \le 3.2 \times 10^6$ and a NaCl concentration of 1N) [48]. Hence, the prefactor $1/\zeta(3\nu)$ becomes 0.54 for $\nu = 0.61$, and 0.49 for $\nu = 0.57$. Consequently, the Zimm relaxation time varies in

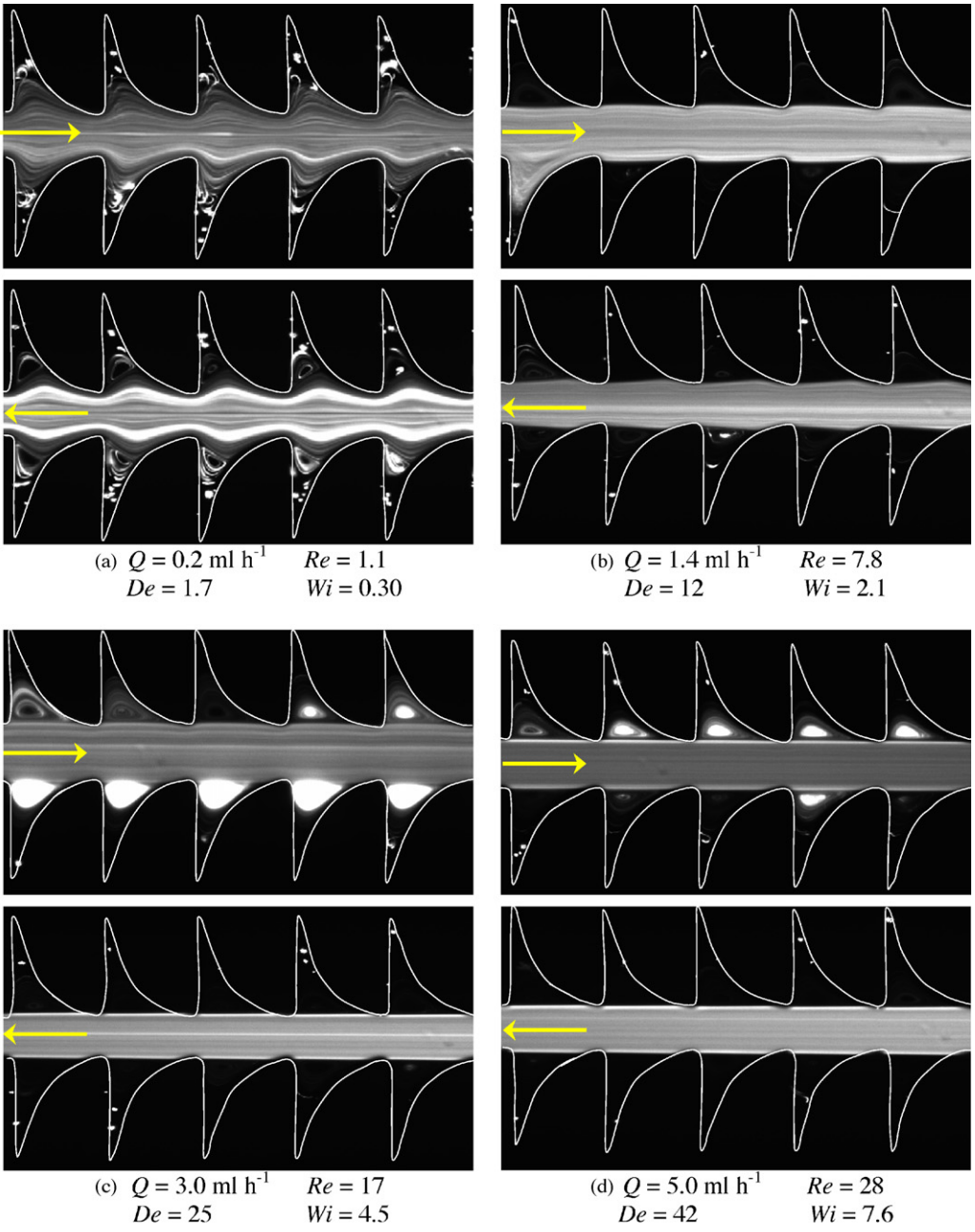

Fig. 11. Effect of elasticity on the flow patterns of the PEO-8M 100 fluid (microchannel C_1) at 298.4 K.

the range between 9.8 and 10.8 ms, which is similar to the value found from the CaBER experiments for the same fluid. For quantitative purposes, in the calculation of the dimensionless numbers, we will use in all cases the CaBER relaxation time.

Table 5 provides the coil overlap concentration (c^*), the dimensionless concentration (c/c^*) and the Zimm relaxation time (λ_{Zimm}) obtained at the reference temperature (293.2 K), for each fluid used in the experiments.

The PEO-8M 100 and PAA solutions are diluted and therefore the Zimm relaxation time is in reasonable agreement with the measured values. All the other viscoelastic fluids used in this work are semi-dilute solutions. For the PEO-2M and PEO-8M fluids in particular, λ_{Zimm} is smaller than the relaxation time found under capillary break-up extensional measurements which is probably due to molecular chain interactions during the CaBER experiments as described in Rodd et al. [50] and Soulages et al. [51].

For the shear flow rheological characterization, a shear rheometer (Anton Paar, model Physica MCR301) was used with a cone-plate geometry (75 mm diameter and 1° angle) operating in the shear rate range of $1 \leq \dot{\gamma}/s^{-1} \leq 7 \times 10^3$. For all polymer solutions, the shear viscosity (η) was measured at different temperatures ranging from 283.2 K to 303.2 K and the time-temperature superposition principle was used in order to obtain a master curve. The corresponding shift factor is defined as [52]:

$$a_T = \frac{\eta(T)}{\eta(T_0)} \frac{T_0}{T} \frac{\rho_0}{\rho} \tag{3}$$

where $\eta(T)$ is the shear viscosity at a given absolute temperature T, $\eta(T_0)$ is the shear viscosity at the reference absolute temperature T_0 (293.2 K), whereas ρ_0 and ρ are the fluid densities at the reference temperature and at temperature T, respectively. For the range of temperatures used in the measurements, the variation of the fluid

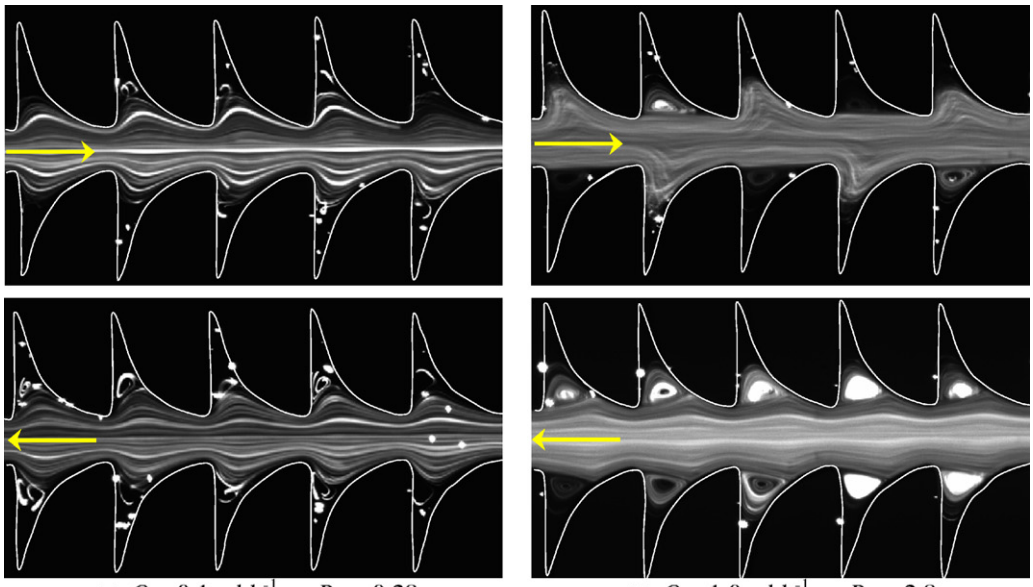

(a) $Q = 0.1$ ml h^{-1} $Re = 0.28$ $De = 4.5$ $Wi = 0.82$

(b) $Q = 1.0$ ml h^{-1} $Re = 2.8$ $De = 45$ $Wi = 8.2$

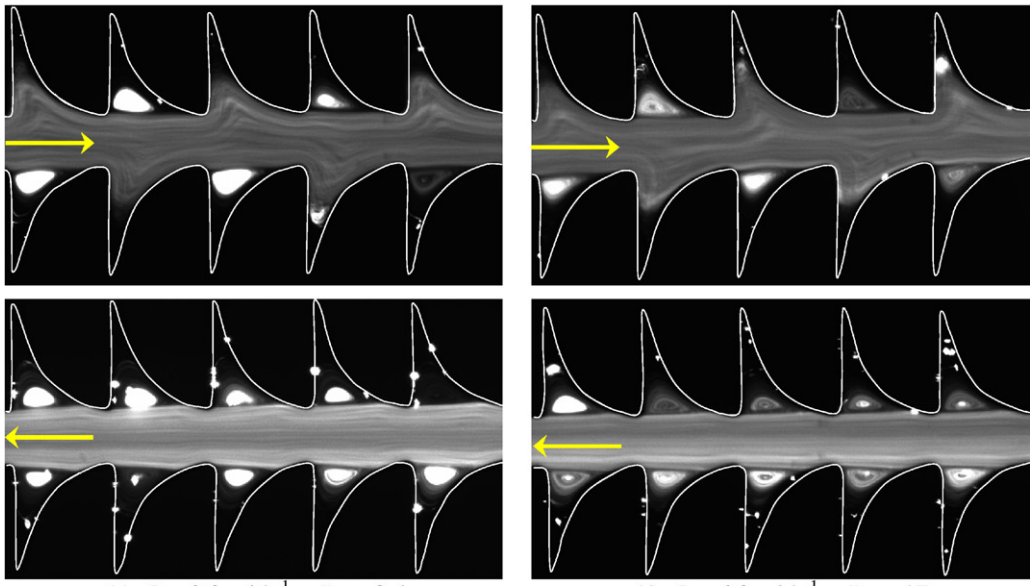

(c) $Q = 3.0$ ml h^{-1} $Re = 8.4$ $De = 135$ $Wi = 25$

(d) $Q = 6.0$ ml h^{-1} $Re = 17$ $De = 270$ $Wi = 50$

Fig. 12. Effect of elasticity on the flow patterns of the PAA fluid (microchannel C_1) at 298.5 K.

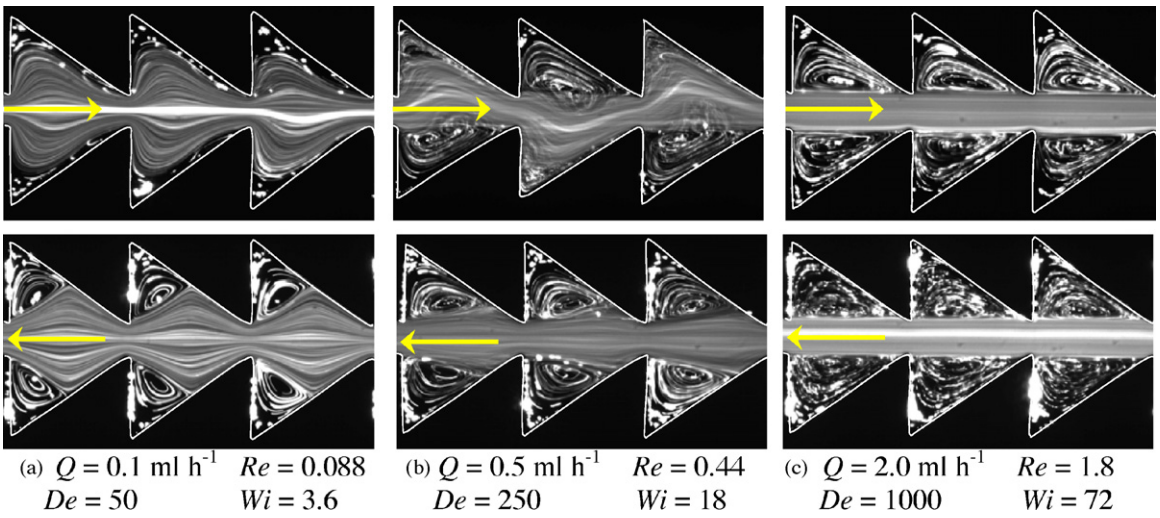

Fig. 13. Flow patterns of the PEO-8M fluid flow in the microchannel with a triangular shape (T) at 298.4 K.

density is negligibly small, hence the shift factor can be calculated through the following expression [52]:

$$a_T = \frac{\eta(T)}{\eta(T_0)} \tag{4}$$

The dependency of the shift factor on the temperature can be described by an Arrhenius equation:

$$\ln(a_T) = \frac{\Delta H}{R}\left(\frac{1}{T} - \frac{1}{T_0}\right) \tag{5}$$

where ΔH represents the activation energy for flow and R the universal gas constant.

In order to determine the master curve, the shear viscosity and the shear rate need to be calculated in the reduced form or transformed to the reference temperature according to:

$$\eta_r = \eta(T_0) = \frac{\eta(T)}{a_T} \tag{6}$$

$$\dot{\gamma}_r = \dot{\gamma}(T_0) = a_T\dot{\gamma} \tag{7}$$

The master curves for steady shear flow are shown in Fig. 3a for the PEO solutions and in Fig. 3b for the PAA solution. In addition, the fit of the simplified Phan–Thien–Tanner (sPTT) model [53], with a solvent contribution, which predicts a shear-thinning behavior is also shown. More details about this viscoelastic model can be found in Ref. [51] or on the original Ref. [53].

Table 7
Critical conditions for the onset of diodicity in the C_1 hyperbolic microchannel, and average temperature of the experiments.

Fluid	Q_{crit} (ml h^{-1})	T (K)	De_{crit}	Wi_{crit}
PEO-2M	0.13	293.1	4.1	0.74
PEO-8M	0.08	292.1	23	4.3
PEO-8M + Glyc.	0.35	295.4	23	4.1
PEO-8M 100	0.80	298.7	6.6	1.2
PAA	0.04	298.8	1.8	0.33

In the PTT model, ε is an extensibility parameter that influences the extensional viscosity, η_P is the zero-shear viscosity of the polymer and η_s is the solvent viscosity. The zero-shear viscosity of the model in shear flow is simply given by: $\eta_0 = \eta_P + \eta_s$ and the solvent viscosity ratio is given by $\beta = \eta_s/\eta_0$. Here the parameter of the model related to the second normal stress difference, ξ, was kept equal to zero. Table 6 presents the rheological parameters of the sPTT model used in this work, including the Arrhenius equation parameter $\Delta H/R$ (cf. Eq. (5)).

In the fitting of the sPTT model we used the relaxation time obtained in the CaBER measurements (cf. Table 4). We fitted the

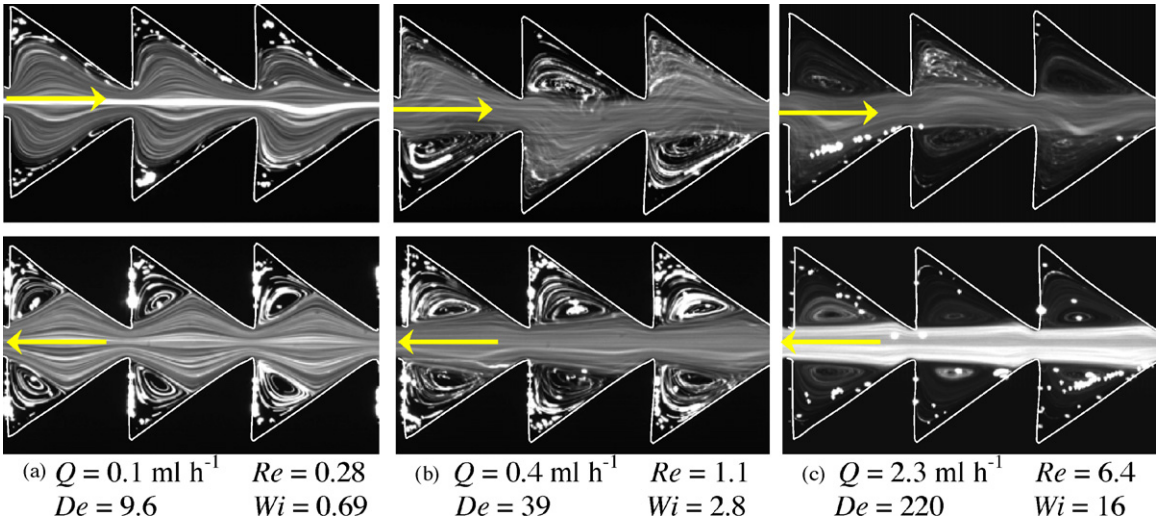

Fig. 14. Flow patterns of the PAA fluid flow in the microchannel with a triangular shape (T) at 298.5 K.

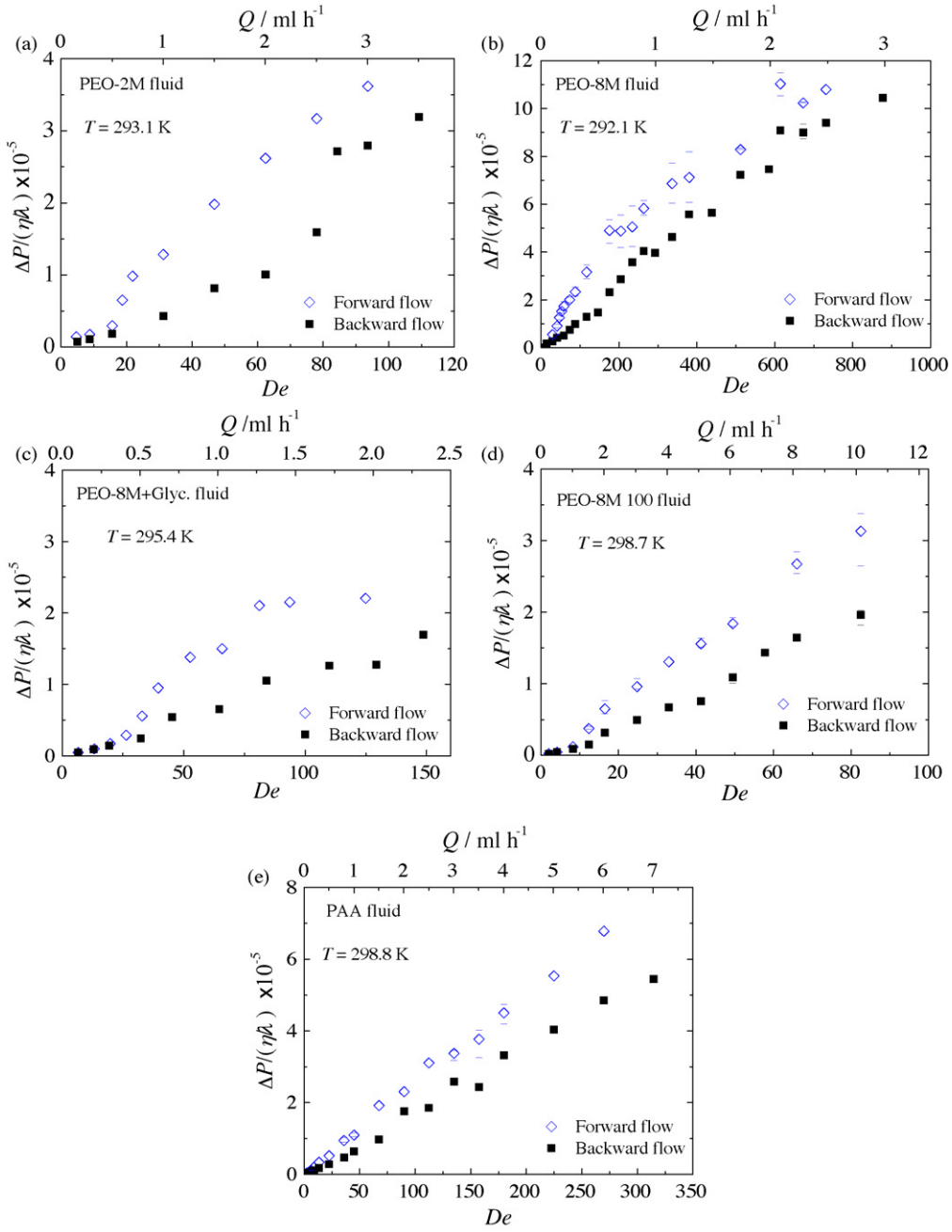

Fig. 15. Dimensionless pressure drops in the forward and backward directions of microchannel C_1, as a function of the flow rate and Deborah number for: (a) PEO-2M, (b) PEO-8M, (c) PEO-8M + Glyc., (d) PEO-8M 100 and (e) PAA.

rheological data to this model and report the corresponding values in Table 6, in order to be possible to perform numerical simulations of the experiments here presented in future works.

3.2. Relevant dimensionless numbers

In addition to the Hencky strain, defined in Section 2.1 as $\varepsilon_H = \ln(D_1/D_2)$, other dimensionless numbers are relevant for this work. The Reynolds number is defined here as

$$\mathrm{Re} = \frac{\rho V_2 D_2}{\eta_0} \tag{8}$$

where V_2 is the mean velocity at the channel throat (with dimension D_2) (cf. Fig. 1).

The flow of the viscoelastic fluids is also characterized using a Deborah (De) or a Weissenberg (Wi) number:

$$\mathrm{De} = \lambda\dot{\gamma} = \frac{\lambda V_2}{D_2/2} \tag{9}$$

$$\mathrm{Wi} = \lambda\dot{\varepsilon} = \lambda\frac{V_2 - V_1}{L} \tag{10}$$

in which the characteristic shear rate is estimated using the narrow dimension of the channels $\dot{\gamma} = V_2/(D_2/2)$. The Weissenberg number is expressed in terms of the strain rate ($\dot{\varepsilon}$) along the microchannel, where V_2 and V_1 correspond to the average velocity at positions corresponding to D_2 and D_1, respectively, separated by a distance L. The corresponding elasticity number is independent of flow rate and is defined as $\mathrm{El} = \mathrm{De}/\mathrm{Re} = 2\lambda\eta_0/\rho D_2^2$, assuming a constant value for each fluid/geometry combination.

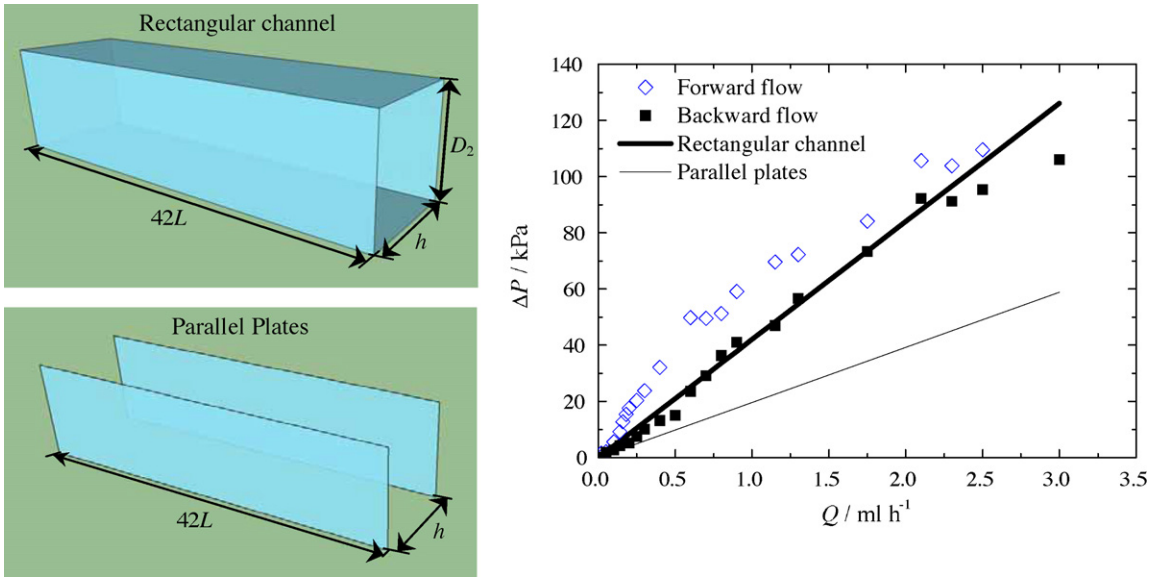

Fig. 16. Pressure drop as a function of the flow rate for the PEO-8M fluid flow. Comparison with the pressure drop estimated for flow in a rectangular channel and between two parallel plates.

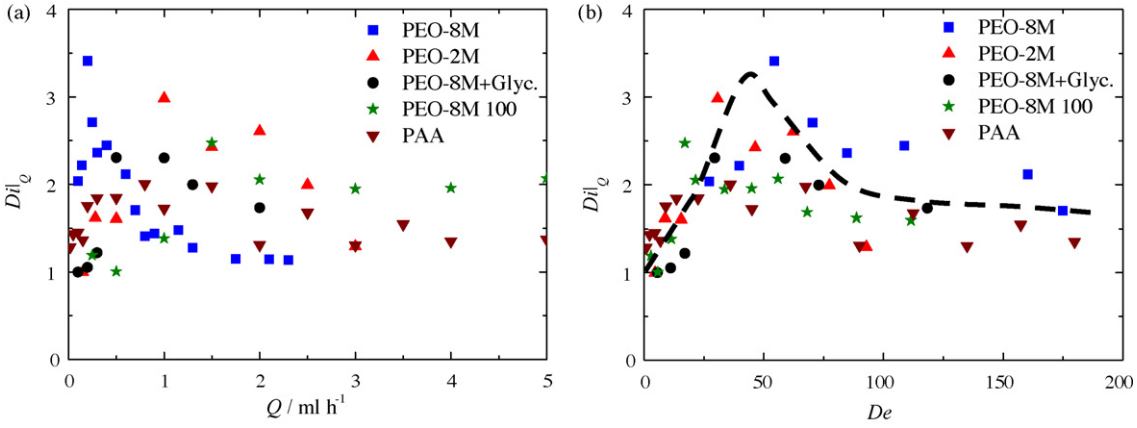

Fig. 17. Diodicity (in terms of pressure drop ratio) as a function of flow rate (a) and Deborah number (b) for all viscoelastic fluids used. The dashed line in (b) is a guide to the eye.

The diodicity of the microchannels can be evaluated at a constant flow rate value, here defined as

$$\mathrm{Di}|_Q = \frac{\Delta P_{\mathrm{Forward}}}{\Delta P_{\mathrm{Backward}}} \tag{11}$$

where $\Delta P_{\mathrm{Forward}}$ is the pressure drop in the forward direction and $\Delta P_{\mathrm{Backward}}$ is the pressure drop in the backward direction for the same flow rate Q. Alternatively, rectification effects can also be calculated at a constant pressure drop value:

$$\mathrm{Di}|_{\Delta P} = \frac{Q_{\mathrm{Backward}}}{Q_{\mathrm{Forward}}} \tag{12}$$

where Q_{Backward} and Q_{Forward} are the flow rates in the backward and forward flow directions for the same total pressure drop, ΔP, respectively.

4. Results and discussion

Initially, a preliminary investigation was carried out on the flow of a single viscoelastic fluid in all hyperbolic microchannels in order to identify the most efficient rectifier under negligible inertia. Subsequently, the best geometry is investigated more extensively with all Newtonian and non-Newtonian fluids described in Section 3.1. Finally, the performance of the chosen geometry is compared with that of the triangular nozzle/diffuser rectifier proposed by Groisman and Quake [37].

4.1. Preliminary study

The flow of a single viscoelastic fluid was studied in the four hyperbolic microchannels C_1, C_2, C_3 and C_4 (cf. Section 2.1) with the aim of establishing the most efficient microfluidic rectifier. The non-Newtonian fluid used for comparison purposes was the 0.1 wt.% aqueous solution of PEO-8M. Fig. 4 shows the pressure drop measured as a function of the flow rate for both flow directions.

The results show a similar qualitative behavior in all microgeometries. At low flow rates the flow is quasi-Newtonian and reversible (negligible diodicity) and the pressure drop increases linearly with the flow rate. However, above a critical flow rate value (Q_{crit}), which is geometry-dependent, the pressure drop increases nonlinearly with Q (or De). The critical conditions are $Q_{\mathrm{crit}} \sim 0.08\ \mathrm{ml\,h^{-1}}$ for channel C_1, $Q_{\mathrm{crit}} \sim 0.3\ \mathrm{ml\,h^{-1}}$ for channel C_2, $Q_{\mathrm{crit}} \sim 0.6\ \mathrm{ml\,h^{-1}}$ for channel C_3 and $Q_{\mathrm{crit}} \sim 0.1\ \mathrm{ml\,h^{-1}}$ for channel C_4. This is a typical behavior of viscoelastic fluid flows through contractions at micro or macro-scales (e.g. [50,54–56]). Further-

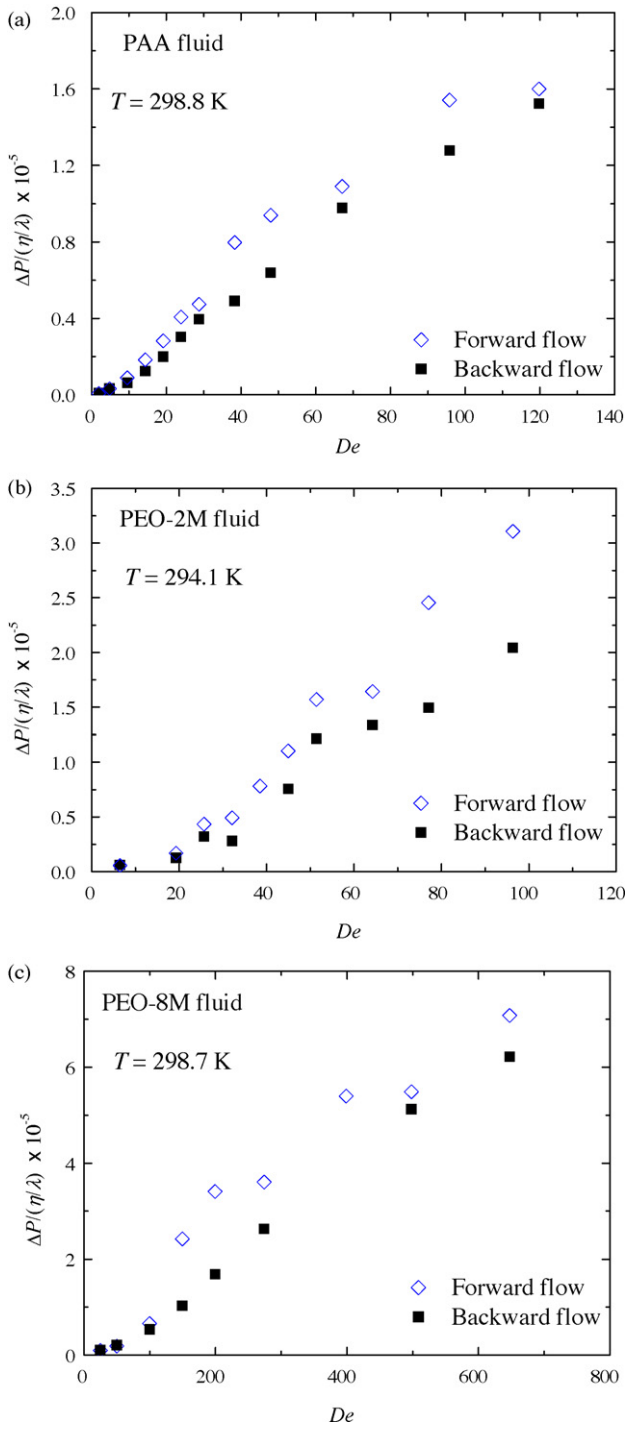

Fig. 18. Dimensionless pressure drop measured in the two flow directions of triangular-shaped channel (T) as a function of the Deborah number for (a) PAA, (b) PEO-2M and (c) PEO-8M fluids.

more, the flow resistance is different in the two flow directions and is higher when the fluid flows along the series of hyperbolic contractions in the forward direction, i.e. when the fluid flows in a quasi-homogeneous stretching extensional flow, than when it flows in the backward direction, in a quasi-homogeneous relaxing extensional flow. As a consequence of this different flow resistance, rectification effects emerge. The corresponding variation of diodicity is shown in Fig. 5 as a function of flow rate for all microchannels studied.

Channels C_1 and C_4 present the highest diodicities at low flow rates, namely at $Q \sim 0.2\,\mathrm{ml\,h^{-1}}$ and $Q \sim 0.35\,\mathrm{ml\,h^{-1}}$, respectively. The maximum diodicities ($Di|_Q$) are in excess of 3 and 2 for channels C_1 and C_4, respectively. For channel C_2, the maximum diodicity is about 2 (at a flow rate, $Q \sim 0.5\,\mathrm{ml\,h^{-1}}$) while for channel C_3, which has the lowest total Hencky strain, the measured diodicity is the lowest (maximum diodicity about 1.5 at $Q \sim 1.7\,\mathrm{ml\,h^{-1}}$).

We anticipated that the highest rectification effects would be observed for the channel with the highest Hencky strain (channel C_4). However, this trend was not observed in the experiments, presumably because for geometry C_4 shear effects become important in the narrow part of the channel, with the boundary layer of the shear flow occupying a significant portion of the duct. This apparent increase in shear effects counteracts the extensional effects that are necessary for the increase of the local pressure drop in the forward direction, with the corresponding increase of rectification effect. Thus, the channel with the best performance corresponds to a compromise between high extension and low shear and it is microgeometry C_1, which exhibits the highest diodicity. We shall focus on this microchannel over the next sections.

4.2. Newtonian fluid flow

Fig. 6 shows the effect of inertia on the visualized pathlines for the Newtonian fluid flow in channel C_1 taken at the center plane of the microgeometry.

At low flow rates ($Re \lesssim 0.6$), there is no significant flow separation and the flow patterns are similar for the two flow directions, due to the flow reversibility characteristic of Newtonian creeping flows. In the range $0.6 \lesssim Re \lesssim 6$ recirculations become visible between the expansion corners and the far corners and increase in size as Re increases for the forward flow direction. When the flow inertia increases further ($Re \gtrsim 6$), large recirculations are visible near the far corner in the forward direction, in agreement with the experimental results of Groisman and Quake [37]. Since the fluid is flowing through a sequence of abrupt expansions, inertia is responsible for the appearance and the subsequent growth of the recirculations, which is in agreement with the results found by Oliveira et al. [42] and Rodd et al. [50] for planar microchannels.

In the backward direction the recirculations also emerge and grow in size in the region between the corners, but these events occurred at Re higher than the corresponding Re in the forward flow direction. In all cases, the increase of the size of the recirculations with Re is limited by spatial confinement. For both flow directions, the fluid in the vicinity of the far corners is essentially stagnant. A similar behavior was also observed in the experiments of Groisman and Quake [37].

In order to assess the Newtonian fluid flow anisotropy, we conducted pressure drop measurements using de-ionized water in two geometries (the hyperbolic C_1, and triangle T microchannels) and for both flow directions. The experiments were carried out for a wide range of flow rates, $Q \lesssim 45\,\mathrm{ml\,h^{-1}}$ ($Re \lesssim 260$) for microchannel C_1 and $Q \lesssim 30\,\mathrm{ml\,h^{-1}}$ ($Re \lesssim 180$) for microchannel T. The results are compiled and compared in Fig. 7.

In the range of flow conditions studied, the pressure drop increases linearly with the flow rate for both microgeometries and flow directions. Furthermore, no rectification effects are found since the pressure drop in the two flow directions essentially coincide at the same flow rate, even at the highest Reynolds numbers measured, which is well inside the nonlinear range where inertial effects are important. Therefore, these microchannels are not efficient for operation with Newtonian fluids.

4.3. Viscoelastic fluid flow

4.3.1. Flow patterns

The flow patterns for all viscoelastic fluids are qualitatively similar as can be assessed from observation of Figs. 8–12, where

representative streak line images are shown to highlight the effects of the Deborah number and flow direction.

At low flow rates, viscous effects are dominant and the flow patterns (Figs. 8a, 9a, 10a, 11a and 12a) are similar to those obtained with the Newtonian fluid (Fig. 6), i.e. they are identical for both flow directions rendering the flow fully reversible and rectification effects entirely absent.

Above a certain flow rate (or a critical Deborah number, De_{crit}), markedly different flow patterns are observed for the two flow directions. For the backward flow direction, regions of separated flow appear near the far corner in all elements of the microgeometry with the flow remaining symmetric and steady (Figs. 8b, c, 9b, 10b, c and 12b, c for backward flow). In this case, the fluid tends to enter inside the hyperbolic corner and the pathlines show a bent shape. The existence of upstream recirculations when a shear-thinning fluid flows through an abrupt contraction is a well-known phenomenon and the results obtained from flow visualizations are consistent with the numerical studies for a 2D channel presented by Alves et al. [57] at the macroscale and the experimental results of McKinley et al. [56] for a microchannel with a hyperbolic shape.

For the forward flow direction, recirculations also emerge near the far corner inside each microchannel element. However, in this case, elastic instabilities appear and the recirculations are only visible in some elements of the microgeometry (Figs. 8c, d, 9a, c, 10c and 12b–d for forward flow direction), appearing and disappearing in time without a clearly discernible pattern. Consequently, due to the onset of this elastic instability, the flow is now asymmetric and unsteady. These instabilities are elastic in nature since inertial effects are not important (low Reynolds number flows). Purely elastic instabilities in microchannels have been studied by Arratia et al. [58] and Poole et al. [59] in cross-slot microchannels, by Oliveira et al. [60] in flow focusing geometries with 3 entrances and by Soulages et al. [51] in T-shaped microgeometries. See also Morozov and van Saarloos [61] and papers within for a discussion on elastic instabilities.

For the backward flow direction, we also observe the onset and enhancement of elastic instabilities (Fig. 8d for backward flow), but these occur at higher flow rates. The nonlinear increase of the flow resistance also occurs above a critical flow rate, but to a smaller extent than those found in the forward flow direction, at least for the range of flow rates studied in our experiments.

Another interesting flow characteristic is that the fluids tend to flow mostly through the central region/portion of the microchannel and the streamlines are no longer curved (cf. Figs. 8a, b, 10a, b, 11a and 12a), becoming progressively rectilinear as the flow rate increases. This phenomenon is observed to some extent for all viscoelastic fluids studied, especially at high Deborah numbers (Figs. 10d and 11b–d).

Streak line images obtained in the triangular-shaped microchannels (inspired by the work of Groisman and Quake [37]) are shown in Fig. 13 for the PEO-8M fluid and in Fig. 14 for the PAA solution.

The flow behavior observed for this microgeometry has some general similarities to that obtained with the hyperbolic geometries for all viscoelastic fluids studied, but also bears some important differences. The forward flows at low De exhibit recirculations near the far corner, and show small lip vortices emerging in the vicinity of the throat (Figs. 13a and 14a), whereas in the backward direction, the recirculations become visible at lower flow rates than in the forward direction (Figs. 13a and 14a). Increasing De, elastic effects become important, and instabilities appear in the forward flow direction (Figs. 13b and 14b, c) leading to unstable flow. When De is increased further, the pathlines become symmetric, steady and are similar for the two flow directions (Fig. 13c). These results are in agreement with the findings of Groisman and Quake [37] in a geometry with the same shape (the only difference here is the smaller depth of 50 μm as compared with 100 μm in their study).

4.3.2. Pressure drop

Fig. 15 presents the variation of the dimensionless pressure drop with flow rate measured in channel C_1 for all non-Newtonian fluids considered. The flow resistance behavior in the two flow directions is analogous for all viscoelastic fluids and resembles the preliminary results presented in Section 4.1. At low De, the flow is quasi-Newtonian and reversible, but above a critical value (De_{crit}) the dimensionless pressure drop increases sharply with the flow rate and starts to differ in the forward and backward directions, being invariably larger in the former.

The flow rate at the transition point in the pressure drop profile is significantly different for all fluids studied, as illustrated in Table 7, which stems from the different fluid rheology. In Table 7 the corresponding critical Deborah numbers, calculated with the relaxation time at the temperature of the experiments, are included. These relaxation times were determined from the values measured with the CaBER at $T = 293.2$ K and then corrected to the temperature of the experiments using the time-temperature superposition principle (cf. Section 3.1). In Table 7 we also include the estimated critical Weissenberg number (Wi_{crit}), showing that the critical conditions occur for a Weissenberg number close to the coil-stretch transition, $\lambda\dot{\varepsilon} = 0.5$ [62], in particular for the PAA and the lighter PEO, an indication suggesting that the significant increase in the pressure drop is related to the strong extensional behavior of the flow along the forward direction.

Cross analyzing Table 7 with the flow patterns reported in Section 4.3.1, we conclude that De_{crit} corresponds approximately to the conditions when the flow becomes unsteady in the forward flow direction, and enhanced flow resistance anisotropy sets in due to the elastic instability. When the flow is unsteady we report the average pressure drop, together with the maximum and minimum values measured. These extreme values are reported as horizontal bars (cf. Fig. 15), while the symbols correspond to the time-averaged values.

For the forward direction, the pressure drop variation with flow rate shows a sharp increase above De_{crit}. Thus, the onset of elastic instabilities leads to an enhancement of the flow resistance in the forward direction and as a consequence rectification effects (or diodicity) emerge, since the same flow rate generates significantly different pressure drops in the forward and backward flow directions. When the flow instabilities in the backward direction also emerge, at higher flow rates, the difference between the forward and backward pressure drops decreases, and the rectification effect is reduced.

To better understand the origin of the enhancement of the flow resistance we carried out a simple theoretical analysis which assumes that the main flow occurs primarily in the central region of the microchannel (as shown in Fig. 9b) when elastic effects are important. Under this simplified scenario, the measured flow resistance can be compared with two limiting pure shear flow cases: (i) the flow confined in a rectangular channel with four walls, corresponding to no-slip conditions at the walls and (ii) the flow between two parallel plates spaced 50 μm apart, which corresponds to the depth of the microchannel. Case (i) assumes a no-slip condition at the interface between the main flow and the recirculation, an assumption that is reasonable when the secondary flow in the recirculation is weak, and therefore the velocity of the dividing streamlines (assumed as straight lines) is small. This case corresponds to the flow in a rectangular channel, for which the velocity profile and pressure drop expressions can be found in White [63] for a Newtonian fluid under fully developed flow conditions. The viscoelastic fluids tested have a nearly constant shear viscosity (cf. Fig. 3a), hence these expressions for a Newtonian fluid are ade-

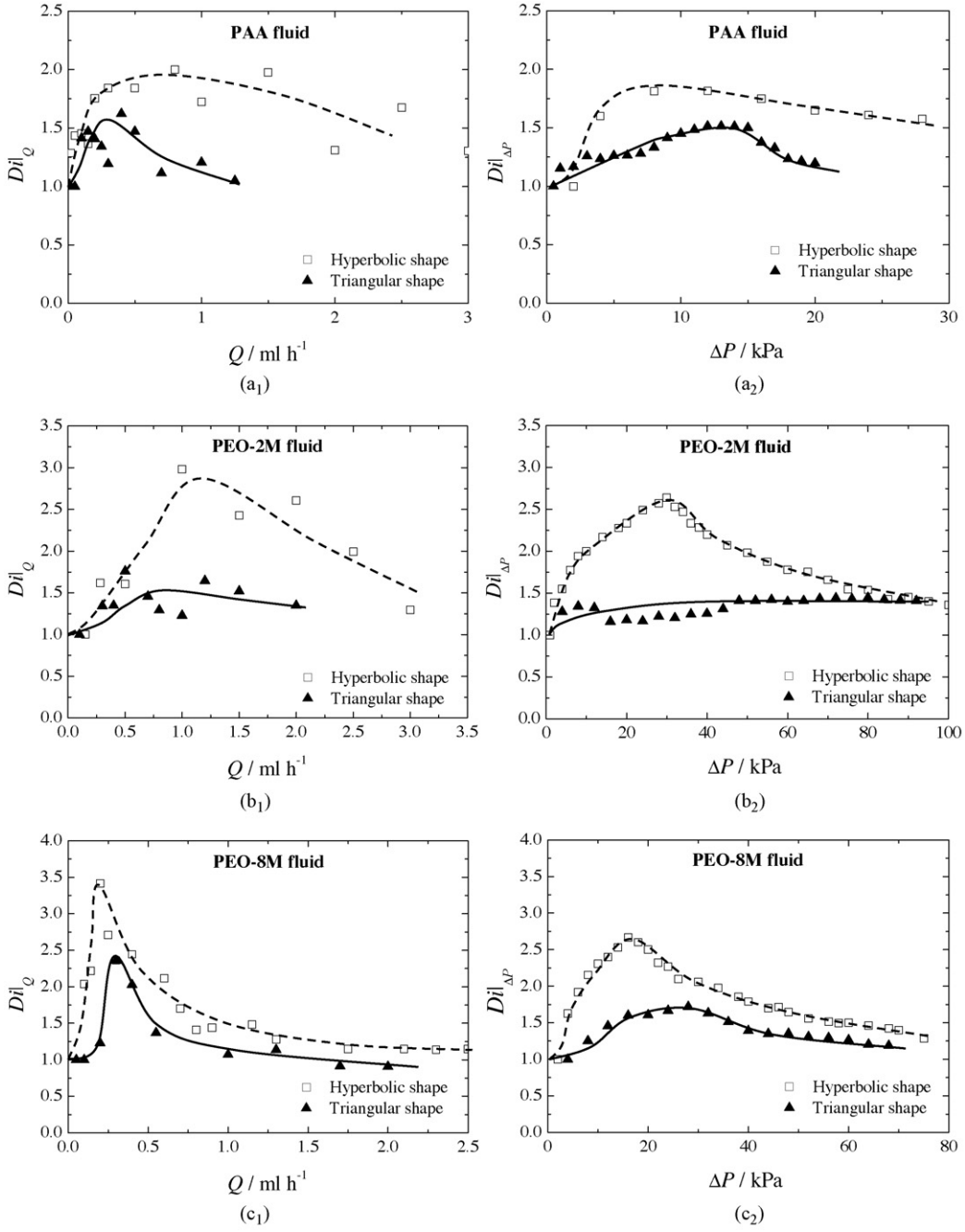

Fig. 19. Comparison between the diodicity obtained with the hyperbolic and triangular microgeometries in terms of pressure drop ratio as a function of the flow rate (left-hand side column) and in terms of flow rate ratio as a function of the pressure drop (right-hand side column). The graphs (a_1) and (a_2) correspond to the fluid PAA, (b_1) and (b_2) to PEO-2M and (c_1) and (c_2) to PEO-8M. The curves are a guide to the eye.

quate (indeed, they are exact for fluids with constant shear viscosity and zero second-normal stress difference, either Newtonian or viscoelastic). The zero-shear viscosity of the viscoelastic fluids was used in the analytical solutions, which is a reasonable estimate due to the weak shear-thinning behavior of the fluids. As an example, for the PAA fluid the decrease of the shear viscosity is only about 15%, in a range of two decades of shear rates. Case (ii) assumes full slip at the dividing streamline, thus the flow field is assumed uniform in the x–y plane (cf. Fig. 1). The bottom and top walls are planar and set 50 μm apart, thus this ideal case corresponds to the flow between two infinite parallel plates. Again, we assume fully developed flow conditions, and Newtonian behavior with a viscosity matching the zero-shear rate viscosity of the fluids. The predictions of these two ideal pure shear flows are shown as solid lines in Fig. 16. When viscoelastic effects are important it is clear that the flow resistance measured in our microfluidic rectifier is higher than that predicted for the two limiting conditions, even higher than for the flow in a rectangular channel, which can be viewed as the upper limit of flow resistance if only shear effects were at play. This gives further credit to the hypothesis that enhanced flow resistance is due primarily to the strong extensional flow along the central region of the microchannel.

In order to compare the diodicity of the flows in the microfluidic device C_1 for the different viscoelastic fluids studied, we plot in Fig. 17 the diodicity calculated in terms of the pressure drop ratio. As can be seen, the 0.1 wt.% aqueous solution of PEO-8M shows the

highest diodicity, achieving a maximum value around 3.5. This fluid has the highest concentration of the heaviest polymer used here. The semi-dilute solution of PEO-2M presents a maximum diodicity of about 3 and the other fluids have rectification effect values in excess of 2, which are all significantly higher than values reported in other studies for viscoelastic fluids in triangular-based geometries [37,40]. When plotted as function of De (or Wi), the diodicity follows a similar trend for all fluids, as shown in Fig. 17b, exhibiting less scatter than Fig. 17a.

In order to make a direct comparison between the results obtained in the hyperbolic rectifier and the triangular geometry proposed by Groisman and Quake [37] it is necessary to use microgeometries with similar aspect ratios and equal depth. This is achieved here by using the microchannel T of Table 1. In Fig. 18a we plot the dimensionless pressure drop as a function of De in the two flow directions for the T microrectifier for the PAA solution, which is similar to the fluid used by Groisman and Quake [37]. Fig. 18b and c display the same quantities in the T microchannel, but for the solutions of PEO-2M and PEO-8M, respectively.

Qualitatively, the variations of the pressure drop with flow rate are similar to those seen for the hyperbolic rectifier, but the difference between the forward and backward pressure drops are clearly smaller. This is better seen in Fig. 19, where the two diodicities ($Di|_{\Delta P}$ and $Di|_Q$) of all comparable cases are plotted.

Since in the experiments we imposed a value of the flow rate and the corresponding pressure drop was measured, we can directly determine the pressure drop ratio for all values of the flow rate considered ($Di|_Q$). On the other hand, to calculate the diodicity in terms of flow rate ratio, it was first necessary to fit the experimental data of ΔP vs Q, in order to allow for the interpolation of the data and the determination of the corresponding flow rate ratio. For this reason, the plot of the $Di|_Q$ vs Q has more scatter (provided from experimental results) than the smoother plot of $Di|_{\Delta P}$ vs ΔP calculated from the fits. In all cases there is a clear advantage of the rectifier with hyperbolic shaped elements both in terms of the ratio between the forward and backward pressure drop for a given flow rate, and also in terms of flow rate ratio, as used by Groisman and Quake [37] in their seminal paper on elasticity driven flow anisotropy under creeping flow conditions.

For the PAA solution, a maximum value of $Di|_Q \approx 2$ is obtained for the hyperbolic geometry while for the triangular geometry a maximum value of approximately 1.6 is observed. In terms of $Di|_{\Delta P}$, the hyperbolic rectifier has a maximum diodicity of about 1.8, while the triangular geometry achieves a maximum value of about 1.5. However, we should emphasize that the value determined here is lower than the values reported by Groisman and Quake [37], due to the difference in channel depth (and consequently of aspect ratio) between their microchannel (100 μm) and ours (50 μm). For the other viscoelastic fluids higher values of $Di|_Q$ and $Di|_{\Delta P}$ were obtained for both rectifiers, but always showing higher diodicity for the hyperbolic shape.

5. Conclusions

The flow of Newtonian and viscoelastic fluids through microfluidic channels that are able to operate as microfluidic rectifiers under creeping flow conditions, was studied. Two different shapes of the microchannels were compared: the nozzle/diffuser arrangement based on triangular elements used in the literature [37] and a new rectifier based on elements with hyperbolic shape [42] that are especially suitable to generate a nearly purely extensional flow.

For Newtonian fluid flow, the flow patterns for both rectifiers are qualitatively similar in the two flow directions and the flow is steady for the wide range of flow rates studied. The pressure drop through the microchannels is found to increase linearly with the flow rate and no noticeable rectification effects were observed even though the maximum Reynolds number achieved for both flow directions was of the order of 250. However, the secondary flow that is induced by flow inertia is found to appear at lower Re for the forward direction, but it has a negligible influence on the pressure drop.

For the polymeric solutions, the pressure drop is also independent of the flow direction at low flow rates, when the flow is quasi-Newtonian. However, due to the viscoelastic nature of the fluids used, increasing the flow rate leads to an anisotropic flow resistance between the two flow directions. At the onset of rectification effects, elastic instabilities emerge in the forward flow direction as the flow becomes unsteady and the flow resistance increases sharply with the flow rate. Although this phenomenon was observed in both types of microgeometries, the hyperbolic shaped microchannels present a higher diodicity. For channels with the same depth (50 μm), the triangular-shaped channel presents a maximum diodicity in terms of pressure drop ratio of about 2.5, whereas the hyperbolic shaped microchannel has a maximum diodicity of 3.5. The hyperbolic shape of the contraction region for forward flow leads to a quasi-ideal extension flow that generates significant increases in pressure drop, thus the maximum diodicity values found for the various viscoelastic fluids are significantly higher than those achieved with the nozzle/diffuser (triangular) geometry proposed by Groisman and Quake [37], and also higher than those reported by Nguyen et al. [40].

Acknowledgements

The authors acknowledge the financial support provided by Fundação para a Ciência e a Tecnologia (FCT) and FEDER through projects PTDC/EQU-FTT/71800/2006, REEQ/262/EME/2005 and REEQ/928/EME/2005. P.C. Sousa would also like to thank FCT for financial support through scholarship SFRH/BD/28846/2006.

References

[1] F.K. Forster, R.L. Bardell, M.A. Afromowitz, N.R. Sharma, A. Blanchard, Design, fabrication and testing of fixed-valve micro-pumps, Proc. ASME Fluids Eng. Div. IMECE FED 234 (1995) 39–44.
[2] D.J. Laser, J.G. Santiago, A review of micropumps, J. Micromech. Microeng. 14 (2004) R35–R64.
[3] M. Nabavi, Steady and unsteady flow analysis in microdiffusers and micropumps: a critical review, Microfluid. Nanofluid. 7 (2009) 599–619.
[4] J.G. Smits, Piezoelectric micropump with 3 valves working peristaltically, Sens. Actuators A 21 (1990) 203–206.
[5] M. Koch, N. Harris, R. Maas, A.G.R. Evans, N.M. White, A. Brunnschweiler, A novel micropump design with thick-film piezoelectric actuation, Meas. Sci. Technol. 8 (1997) 49–57.
[6] M.A. Unger, H.-P. Chou, T. Thorsen, A. Scherer, S.R. Quake, Monolithic microfabricated valves and pumps by multilayer soft lithography, Science 288 (2000) 113–116.
[7] O.C. Jeong, S.S. Yang, Fabrication and test of a thermopneumatic micropump with a corrugated p+ diaphragm, Sens. Actuators A 83 (2000) 249–255.
[8] Q. Cui, C. Liu, X. Zha, Simulation and optimization of a piezoelectric micropump for medical applications, Int. J. Adv. Manuf. Technol. 36 (2008) 516–524.
[9] N. Tesla, Valvular Conduit, US Patent 1329559 (1920).
[10] E. Stemme, G. Stemme, A valveless diffuser/nozzle-based fluid pump, Sens. Actuators A 39 (1993) 159–167.
[11] A. Olsson, G. Stemme, E. Stemme, A valve-less planar fluid pump with 2 pump chambers, Sens. Actuators A 47 (1995) 549–556.
[12] A. Olsson, G. Stemme, E. Stemme, Diffuser-element design investigation for valve-less pumps, Sens. Actuators A 57 (1996) 137–143.
[13] X. Jiang, Z. Zhou, X. Huang, Y. Li, Y. Yang, C. Liu, Micronozzle/diffuser flow and its application in micro valveless pumps, Sens. Actuators A 70 (1998) 81–87.
[14] L.S. Pan, T.Y. Ng, X.H. Wu, H.P. Lee, Analysis of valveless micropumps with inertial effects, J. Micromech. Microeng. 13 (2003) 390–399.
[15] K. Yang, I. Chen, B. Shew, C. Wang, Investigation of the flow characteristics within a micronozzle/diffuser, J. Micromech. Microeng. 14 (2004) 26–31.
[16] V. Singhal, S.V. Garimella, J.Y. Murthy, Low Reynolds number flow through nozzle–diffuser elements in valveless micropumps, Sens. Actuators A 113 (2004) 226–235.
[17] K.W. Oh, C.H. Ahn, A review of microvalves, J. Micromech. Microeng. 16 (2006) R13–R39.

[18] C. Sun, Z.H. Han, Effects of the half angle on the flow rectification of a microdiffuser, J. Micromech. Microeng. 17 (2007) 2031–2038.
[19] S. Tanaka, H. Tsukamoto, K. Miyazaki, Development of diffuser/nozzle based valveless micropumps, J. Fluid Sci. Technol. 3 (2008) 999–1007.
[20] I. Hwang, S. Lee, S. Shin, Y. Lee, J. Lee, Flow characterization of valveless micropump using driving equivalent moment: theory and experiments, Microfluid. Nanofluid. 5 (2008) 795–807.
[21] Y. Wang, J. Hsu, P. Kuo, Y. Lee, Loss characteristics and flow rectification property of diffuser valves for micropump applications, Int J. Heat Mass Transfer 52 (2009) 328–336.
[22] M. Nabavi, L. Mongeau, Numerical analysis of high frequency pulsating flows through a diffuser–nozzle element in valveless acoustic micropumps, Microfluid. Nanofluid. 7 (2009) 669–681.
[23] T. Gerlach, H. Wurmus, Working principle and performance of the dynamic micropump, Sens. Actuators A 50 (1995) 135–140.
[24] M. Heschel, M. Mullenborn, S. Bouwstra, Fabrication and characterization of truly 3D diffuser/nozzle microstructures in silicon, J. Microelectromech. Syst. 6 (1997) 41–47.
[25] A. Olsson, G. Stemme, E. Stemme, Numerical and experimental studies of flat-walled diffuser elements for valve-less micropumps, Sens. Actuators A 84 (2000) 165–175.
[26] H.J. Sheen, C.J. Hsu, T.H. Wu, C.C. Chang, H.C. Chu, C.Y. Yang, U. Lei, Unsteady flow behaviors in an obstacle-type valveless micropump by micro-PIV, Microfluid. Nanofluid. 4 (2008) 331–342.
[27] C.-J. Lee, H.-J. Sheen, Z.-K. Tu, U. Lei, C.-Y. Yang, A study of PZT valveless micropump with asymmetric obstacles, Microsyst. Technol. 15 (2009) 993–1000.
[28] R. Bardell, N. Sharma, F. Forster, M. Afromowitz, R.J. Penny, Designing high-performance micro-pumps based on no-moving parts valves, in: Proc. 1997 ASME Int. Mechanical Engineering Congress and Exposition, Dallas, Texas, 1997.
[29] C. Feldt, L. Chew, Geometry-based macro-tool evaluation of non-moving-part valvular microchannels, J. Micromech. Microeng. 12 (2002) 662–669.
[30] A.R. Gamboa, C.J. Morris, F.K. Forster, Improvements in fixed-valve micropump performance through shape optimization of valves, J. Fluids Eng. 127 (2005) 339–347.
[31] C. Yamahata, C. Lotto, E. Al-Assaf, M.A.M. Gijs, A PMMA valveless micropump using electromagnetic actuation, Microfluid. Nanofluid. 1 (2005) 197–207.
[32] M.C. Carrozza, N. Croce, B. Magnani, P. Dario, A piezoelectric-driven stereolithography-fabricated micropump, J. Micromech. Microeng. 5 (1995) 177–179.
[33] R.H. Liu, Q. Yu, D.J. Beebe, Fabrication and characterization of hydrogel-based microvalves, J. Microelectromech. Syst. 11 (2002) 45–53.
[34] J. Loverich, I. Kanno, H. Kotera, Concepts for a new class of all-polymer micropumps, Lab-on-a-Chip 6 (2006) 1147–1154.
[35] J. Loverich, I. Kanno, H. Kotera, Single-step replicable microfluidic check valve for rectifying and sensing low Reynolds number flow, Microfluid. Nanofluid. 3 (2007) 427–435.
[36] H. Andersson, W. van der Wijngaart, P. Nilsson, P. Enoksson, G. Stemme, A valveless diffuser micropump for microfluidic analytical systems, Sens. Actuators B 72 (2001) 259–265.
[37] A. Groisman, S.R. Quake, A microfluidic rectifier: anisotropic flow resistance at low Reynolds numbers, Phys. Rev. Lett. 92 (9) (2004) 095401–95404.
[38] T.M. Squires, S.R. Quake, Microfluidics: fluid physics at the nanoliter scale, Rev. Mod. Phys. 77 (2005) 126–977.
[39] A. Groisman, M. Enzelberger, S.R. Quake, Microfluidic memory and control devices, Science 300 (2003) 955–958.
[40] N.-T. Nguyen, Y.-C. Lam, S.S. Ho, C.L.-N. Low, Improvement of rectification effects in diffuser/nozzle structures with viscoelastic fluids, Biomicrofluidics 2 (2008) 034101–34114.
[41] J.C. McDonald, D.C. Dufy, J.R. Anderson, D.T. Chiu, H. Wu, G.M. Whitesides, Fabrication of microfluidic systems in poly(dimethylsiloxane), Electrophoresis 21 (2000) 27–40.
[42] M.S.N. Oliveira, M.A. Alves, F.T. Pinho, G.H. McKinley, Viscous flow through microfabricated hyperbolic contractions, Exp. Fluids 43 (2007) 437–451.
[43] C.D. Meinhart, S.T. Wereley, M.H.B. Gray, Volume illumination for two-dimensional particle image velocimetry, Meas. Sci. Technol. 11 (2000) 809–814.
[44] F. Hassouna, S. Morlat-Thérias, G. Mailhot, J.L. Gardette, Influence of water on the photodegradation of poly(ethylene oxide), Polym. Degrad. Stab. 92 (2007) 2042–2050.
[45] V.M. Entov, E.J. Hinch, Effect of a spectrum of relaxation times on the capillary thinning of a filament of elastic liquid, J. Non-Newt. Fluid Mech. 72 (1997) 31–54.
[46] W.W. Graessley, Polymer chain dimensions and the dependence of viscoelastic properties on concentration, molecular weight and solvent power, Polymer 21 (1980) 258–262.
[47] V. Tirtaatmadja, G.H. McKinley, J.J. Cooper-White, Drop formation and breakup of low viscosity elastic fluids: effects of molecular weight and concentration, Phys. Fluids 18 (2006) 043101–43118.
[48] J. Brandrup, E.H. Immergut, E.A. Grulke, Polymer Handbook, 4rd ed., John Wiley & Sons, New York, 1999.
[49] M. Doi, S.F. Edwards, The Theory of Polymer Dynamics, OUP, Oxford, 1986.
[50] L.E. Rodd, T.P. Scott, D.V. Boger, J.J. Cooper-White, G.H. McKinley, The inertio-elastic planar entry flow of low-viscosity elastic fluids in micro-fabricated geometries, J. Non-Newt. Fluid Mech. 129 (2005) 1–22.
[51] J. Soulages, M.S.N. Oliveira, P.C. Sousa, M.A. Alves, G.H. McKinley, Investigating the stability of viscoelastic stagnation flows in T-shaped microchannels, J. Non-Newt. Fluid Mech. 163 (2009) 9–24.
[52] R.B. Bird, R.C. Armstrong, O. Hassager, Dynamics of Polymeric Liquids, vol. 1: Fluid Dynamics, John Wiley & Sons, New York, 1987.
[53] N. Phan-Thien, R.I. Tanner, A new constitutive equation derived from network theory, J. Non-Newt. Fluid Mech. 2 (1977) 353–365.
[54] S. Gulati, S. Muller, D. Liepmann, Direct measurements of viscoelastic flows of DNA in a 2:1 abrupt planar micro-contraction, J. Non-Newt. Fluid Mech. 155 (2008) 51–66.
[55] P.C. Sousa, P.M. Coelho, M.S.N. Oliveira, M.A. Alves, Three-dimensional flow of a Newtonian and Boger fluids in square–square contractions, J. Non-Newt. Fluid Mech. 160 (2009) 122–139.
[56] G.H. McKinley, L.E. Rodd, M.S.N. Oliveira, J.J. Cooper-White, Extensional flows of polymer solutions in microfluidic converging/diverging geometries, J. Cent. South Univ. Technol. 14 (2007) 6–9.
[57] M.A. Alves, P.J. Oliveira, F.T. Pinho, Benchmark solutions for the flow of Oldroyd-B and PTT fluids in planar contractions, J. Non-Newt. Fluid Mech. 110 (2003) 45–75.
[58] P.E. Arratia, C.C. Thomas, J. Diorio, J.P. Gollub, Elastic instabilities of polymer solutions in cross-channel flow, Phys. Rev. Lett. 96 (2006) 144502–144504.
[59] R.J. Poole, M.A. Alves, P.J. Oliveira, Purely elastic asymmetries, Phys. Rev. Lett. 99 (2007) 164503–164504.
[60] M.S.N. Oliveira, F.T. Pinho, R.J. Poole, P.J. Oliveira, M.A. Alves, Purely elastic flow asymmetries in flow-focusing devices, J. Non-Newt. Fluid Mech. 160 (2009) 31–39.
[61] A.N. Morozov, W. van, Saarloos, An introductory essay on substantial instabilities and the transition to turbulence in viscoelastic parallel shear flows, Phys. Rep. 447 (2007) 112–143.
[62] R.G. Larson, J.J. Magda, Coil-stretch transitions in mixed shear and extensional flows of dilute polymer solutions, Macromolecules 22 (1989) 3004–3010.
[63] F.M. White, Fluid Mechanics, 5th ed., McGraw-Hill, Boston, 2003.